atmosphere

MDPI

Article

A Three-Year Climatology of the Wind Field Structure at Cape Baranova (Severnaya Zemlya, Siberia) from SODAR Observations and High-Resolution Regional Climate Model Simulations during YOPP

Günther Heinemann [1,*], Clemens Drüe [1] and Alexander Makshtas [2]

[1] Department of Environmental Meteorology, University of Trier, 54286 Trier, Germany; druee@uni-trier.de
[2] Air-Sea Interaction Department, Arctic and Antarctic Research Institute (AARI), 199397 St. Petersburg, Russia; maksh@aari.ru
* Correspondence: heinemann@uni-trier.de; Tel.: +49-651-201-4623

Abstract: Measurements of the atmospheric boundary layer (ABL) structure were performed for three years (October 2017–August 2020) at the Russian observatory "Ice Base Cape Baranova" (79.280° N, 101.620° E) using SODAR (Sound Detection And Ranging). These measurements were part of the YOPP (Year of Polar Prediction) project "Boundary layer measurements in the high Arctic" (CATS_BL) within the scope of a joint German–Russian project. In addition to SODAR-derived vertical profiles of wind speed and direction, a suite of complementary measurements at the observatory was available. ABL measurements were used for verification of the regional climate model COSMO-CLM (CCLM) with a 5 km resolution for 2017–2020. The CCLM was run with nesting in ERA5 data in a forecast mode for the measurement period. SODAR measurements were mostly limited to wind speeds <12 m/s since the signal was often lost for higher winds. The SODAR data showed a topographical channeling effect for the wind field in the lowest 100 m and some low-level jets (LLJs). The verification of the CCLM with near-surface data of the observatory showed good agreement for the wind and a negative bias for the 2 m temperature. The comparison with SODAR data showed a positive bias for the wind speed of about 1 m/s below 100 m, which increased to 1.5 m/s for higher levels. In contrast to the SODAR data, the CCLM data showed the frequent presence of LLJs associated with the topographic channeling in Shokalsky Strait. Although SODAR wind profiles are limited in range and have a lot of gaps, they represent a valuable data set for model verification. However, a full picture of the ABL structure and the climatology of channeling events could be obtained only with the model data. The climatological evaluation showed that the wind field at Cape Baranova was not only influenced by direct topographic channeling under conditions of southerly winds through the Shokalsky Strait but also by channeling through a mountain gap for westerly winds. LLJs were detected in 37% of all profiles and most LLJs were associated with channeling, particularly LLJs with a jet speed $\geq$ 15 m/s (which were 29% of all LLJs). The analysis of the simulated 10 m wind field showed that the 99%-tile of the wind speed reached 18 m/s and clearly showed a dipole structure of channeled wind at both exits of Shokalsky Strait. The climatology of channeling events showed that this dipole structure was caused by the frequent occurrence of channeling at both exits. Channeling events lasting at least 12 h occurred on about 62 days per year at both exits of Shokalsky Strait.

Keywords: low-level jets; SODAR; atmospheric boundary layer; topographic flow; atmospheric modeling; Laptev Sea

Citation: Heinemann, G.; Drüe, C.; Makshtas, A. A Three-Year Climatology of the Wind Field Structure at Cape Baranova (Severnaya Zemlya, Siberia) from SODAR Observations and High-Resolution Regional Climate Model Simulations during YOPP. *Atmosphere* **2022**, *13*, 957. https://doi.org/10.3390/atmos13060957

Academic Editors: John Walsh, Uma S. Bhatt and Muyin Wang

Received: 16 April 2022
Accepted: 9 June 2022
Published: 12 June 2022

1. Introduction

The Year of Polar Prediction (YOPP) is part of the Polar Prediction Project (PPP) of the World Meteorological Organization (WMO), Geneva, Switzerland, for 2013–2022 with the goal to improve weather forecast and climate modeling in polar regions. YOPP was

launched in mid-2017 and had three special/targeted observing periods in the Arctic: February to March 2018, July to September 2018 and spring 2020 [1]. The latter period is associated with the Multidisciplinary Drifting Observatory for the Study of Arctic Climate (MOSAiC) drift from October 2019 to September 2020 [2]. On the observational side, the goal of YOPP was to increase the number of routine observations (e.g., the frequency of radiosonde launches, see [3]) and to perform additional measurements (e.g., [4]). On the modeling side, process-based model evaluation is one of the key goals of YOPP [1] since the representation of processes in polar regions is a major challenge for weather forecasts and climate models, particularly regarding the atmospheric boundary layer (ABL) and clouds [5–8].

In the present paper, we present ABL measurements and model evaluations for the Russian observatory "Ice Base Cape Baranova" (CB) in the Laptev Sea (Figure 1, Supplementary Material Figure S1). The measurements were performed within the scope of the Changing Arctic Transpolar System (CATS) project for three years (October 2017–August 2020) and cover the complete YOPP period, as well as the period of the MOSAiC drift. The measurements at Cape Baranova (79.280° N, 101.620° E) were carried out by the University of Trier, Trier, Germany, and the Arctic and Antarctic Research Institute (AARI), St. Petersburg, Russia, and were endorsed as part of the YOPP project "Boundary layer measurements in the high Arctic" (CATS_BL, https://apps3.awi.de/YPP/endorsed/projects (accessed on 15 April 2022)). The observatory is located on Bolshevik Island, which is the southernmost island of the Severnaya Zemlya Archipelago (Figure 2). Flow channeling during conditions of a stable boundary layer (SBL) can be expected due to the topography on both sides of Shokalsky Strait between Bolshevik Island and October Revolution Island (Figure 2b). This may lead to enhanced atmosphere–ice–ocean interactions. The region at the northern exit of Shokalsky Strait is known to be an area with large polynya activity and ice production [9]. An example of such a polynya can be seen in Figure 1.

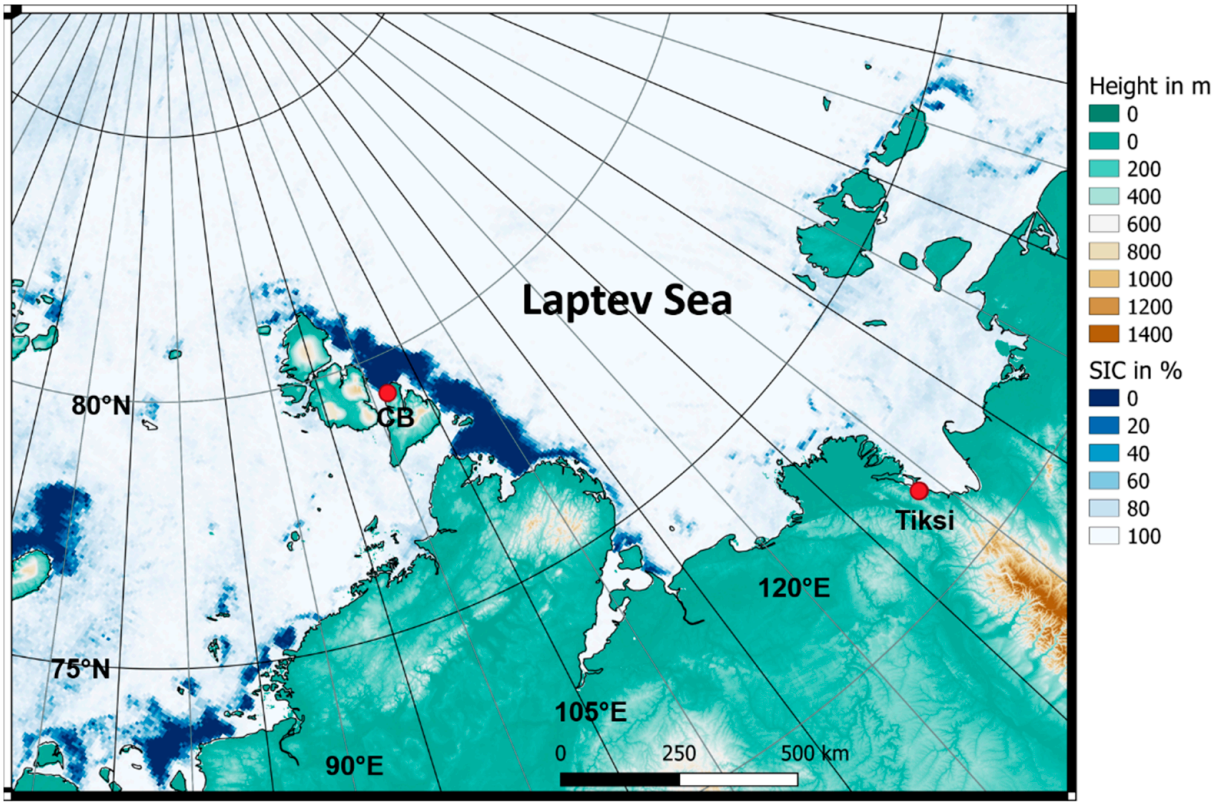

Figure 1. Model domain of the COSMO-CLM (CCLM) model with a 5 km resolution with topography and sea ice concentration for 23 April 2020. The Russian observatories near Tiksi and at Cape Baranova (CB) are marked by red dots.

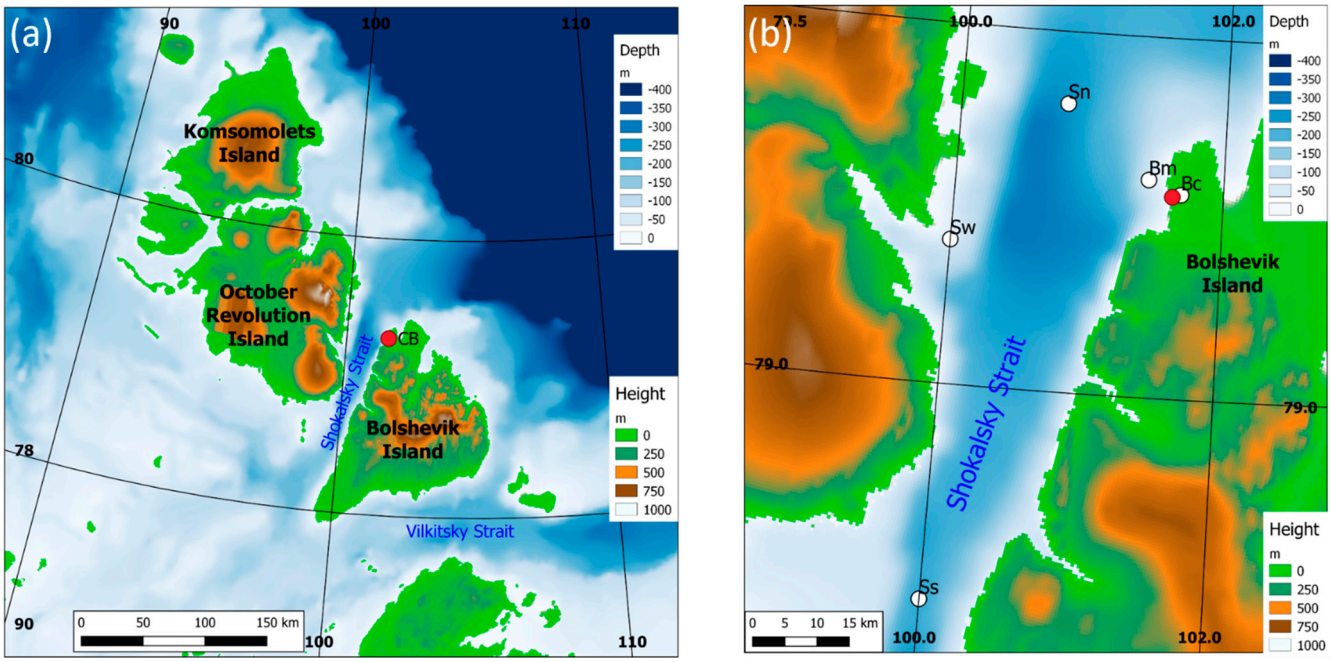

Figure 2. (**a**) Map of the Severnaya Zemlya Archipelago with its topography. The position of Cape Baranova (CB) is marked. (**b**) Zoomed-in image for the Shokalsky Strait. White dots mark positions of selected model grid points: Bc—closest grid point to CB, Bm—closest grid point to CB over the ocean, Sn—Shokalsky north, Sw—Shokalsky west, Ss—Shokalsky south.

The research motivation of the experiment was to contribute to YOPP by generating a high-resolution long-term data set of the ABL structure in the high Arctic using SODAR (Sound Detection And Ranging) measurements for the verification of regional climate models and process studies. A special focus was on topographic flow and low-level jets (LLJs). A detailed description of the data is given in Section 2.

A recent investigation of LLJs in the Laptev Sea area is shown in [10]. Using SODAR data at the Tiksi observatory for the winter of 2014/15, they showed that LLJs are present in about 23% of all profiles with a mean jet speed and height of about 7 m/s and 240 m, respectively. In 3.4% of all profiles, LLJs exceeding 10 m/s occurred. A climatology of LLJs using reanalysis data with 30 km resolution for the years 2000–2010 by [11] showed that the highest frequency of LLJs was associated with strong gradients in topography (e.g., more than 80% for the slopes of the Greenland ice sheet, where katabatic winds dominated. For the Laptev Sea area, the LLJ frequency was much lower (20%) and the LLJs were weaker. However, the resolution of 30 km in their study could not resolve topographic effects in Shokalsky Strait, which has a width of about 20 km at its narrowest point (Figure 2b).

Flow channeling at Smith Sound in the Nares Strait between Canada and Greenland, where the surrounding mountains are higher and the width is larger than for Shokalsky Strait, was shown by [12] in an experimental study using aircraft data. Strong LLJs exceeding 20 m/s were observed. The gap flow in Nares Strait was investigated by several model studies. Ref. [13] used the Polar MM5 model with a 6 km resolution for two years and found monthly mean 10 m winds through Smith Sound of 10 m/s in winter and mostly weak winds during summer. Ref. [14] compared ERA5 data [15] and the ECMWF operational analyses with a 9 km resolution for winter 2016 for this region and concluded that a horizontal resolution lower than 30 km is necessary to represent the flow channeling in Nares Strait. Ref. [16] used the CCLM with a horizontal resolution of 15 km for an analysis of wind extremes for the whole Arctic for the winters of 1979–2016. They found the most extreme winds near Greenland and showed a 95%-tile of more than 20 m/s for Smith Sound. A more detailed climatology of LLJs in Nares Strait for winters 1987–2016 was shown by [17]. They also used the CCLM with 15 km resolution and found a mean 10 m

wind speed of around 12 m/s at the southern exit of Smith Sound. This wind maximum was associated with LLJs typically occurring at 100–250 m in height.

For the region of interest in the present study (Figure 2), a high model resolution of less than 15 km was necessary. The results of [16] with a 15 km resolution showed only a weak signal of flow channeling in Shokalsky Strait and Vilkitsky Strait. In a case study of a storm event in November 2013 using the CCLM with a 5 km resolution by [18], a pronounced wind maximum of more than 16 m/s was found at the northern exit of Shokalsky Strait. A recent study for the Laptev Sea using the CCLM with a 12 km resolution for 1980–2016 by [19] showed wind maxima of about 7 m/s associated with the mountains of the Severnaya Zemlya islands, which were attributed to downslope windstorms.

In the present paper, we present a three-year climatology of the wind field structure at Cape Baranova using SODAR observations and CCLM simulations with 5 km resolution.

2. Materials and Methods

2.1. Near-Surface Measurements and General Meteorological Conditions

At the observatory, standard meteorological near-surface quantities are measured at a meteorological tower (Table 1, Supplementary Material Figure S2). Data are stored with a 3 h resolution in the data archive of the AARI. Figure 3 gives an overview of the meteorological conditions during the investigation period October 2017–August 2020. The temperature showed a pronounced yearly cycle, with a minimum of −39.0 °C and a maximum of 15.9 °C. In the Arctic winter (November–April), the temperature was typically below −10 °C (median of −11.7 °C) and 25% of the data were below −22.0 °C. The wind showed no yearly cycle, the maximum was 31.0 m/s and the mean was 6.2 m/s (75%-tile was 9.0 m/s).

Table 1. Instruments and measurements at Cape Baranova used for this study.

Instrument	Variable	Height/Range	Frequency	Owner
SODAR MFAS (Scintec)	3D wind profile, wind variances	30 m–400 m	20 min/1 h	University Trier
windRASS extension (Scintec)	Temperature profile	40 m–400 m	20 min/1 h	University Trier
Radiosonde	Wind, humidity and tem perature profile	0–25 km	12–24 h	Roshydromet
Tower	Wind (speed and direction) Temperature and humidity	10 m 2, 8 m	3 h	Roshydromet

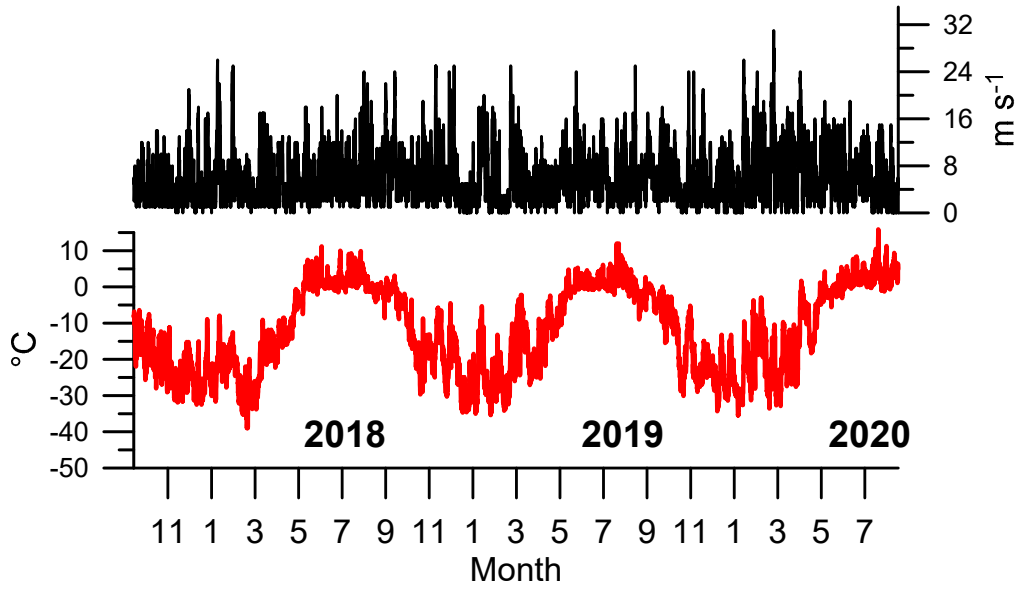

Figure 3. Time series of the 2 m temperature (red line) and 10 m wind speed during the investigation period (3 h values).

The wind rose for the 10 m wind (Figure 4a) showed that the southwesterly winds were predominant, that is, along the axis of Shokalsky Strait, which indicated that flow channeling was present. The highest wind speeds also occurred in the southwesterly direction. The wind speed distribution (Figure 4b) showed a maximum of approximately 2 m/s and a long tail for large wind speeds.

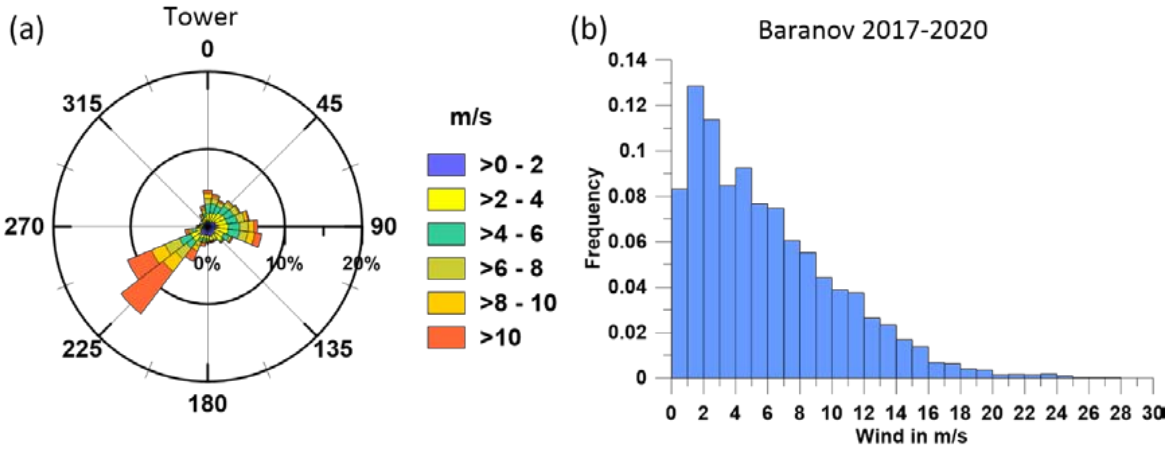

Figure 4. (**a**) Wind rose (15° bins) for the 10 m wind and (**b**) frequency distribution of the 10 m wind for October 2017–August 2020.

2.2. SODAR Measurements

From 14 October 2017 to 1 September 2020, SODAR with an additional RASS (radio acoustic sounding system) was installed alongside the existing instrumentation at Cape Baranova (Supplementary Material Figure S3, Table 1). The SODAR measured the wind profiles in the lowest 400 m via the Doppler shift of sound returns (frequencies between 1650 Hz to 2750 Hz). The RASS measured the virtual temperature profile in the lowest 400 m using the speed of sound (we used the WindRASS system only as a conventional RASS measuring temperatures and not for the wind profile). The profiles were measured with a 10 m vertical resolution every 20 min and were averaged over one hour. For details of the SODAR/RASS system and data quality control, see [10]. The SODAR/RASS was installed about 500 m east of the main observatory, where the routine synoptic observations and radiosonde launches were performed (Supplementary Material Figure S1). The SODAR/RASS site was a distance of approximately 600 m from the coastline, while the meteorological tower was located at a distance of approximately 100 m from the coastline.

An overview of the SODAR/RASS measurements is shown in Figure 5. Due to a failure of the power unit, the whole system did not measure from 7 June to 15 December 2019. Cape Baranova can be reached only a few times each year, and the delivery of spare parts from Germany to Russia, including customs formalities, took a long time. The RASS measurements worked well during the first six months, but then the RASS data availability degraded significantly and it worked only for short periods. This was probably due to a lack of readjustment of the RASS antennas, which would have been necessary at the beginning of the thawing period. The same problem was encountered by [10] during RASS measurements for one year at Tiksi. For short periods, a correct adjustment of the RASS antennas could be achieved, but due to the large data gaps, the RASS data were not used for the present study. SODAR measurements are disturbed for wind velocities near the ground exceeding 10 m/s because the signal-to-noise ratio becomes poor due to wind-induced noise and beam drift (away from the antenna) [20]. This leads to data gaps and limits the vertical range. While at a height of 50 m, SODAR data are available for 52% of all hours, the availability decreased to 45% at 100 m, 28% at 200 m and 15% at 300 m. The data availability was the highest for the first winter season in 2017/18 (Supplementary Material Figure S4) when about 80% of the data were available at lower levels and more than 30%

even at 300 m in height. During the winter of 2018/19, the data availability was lower by about 20% at all levels (Supplementary Material Figure S4).

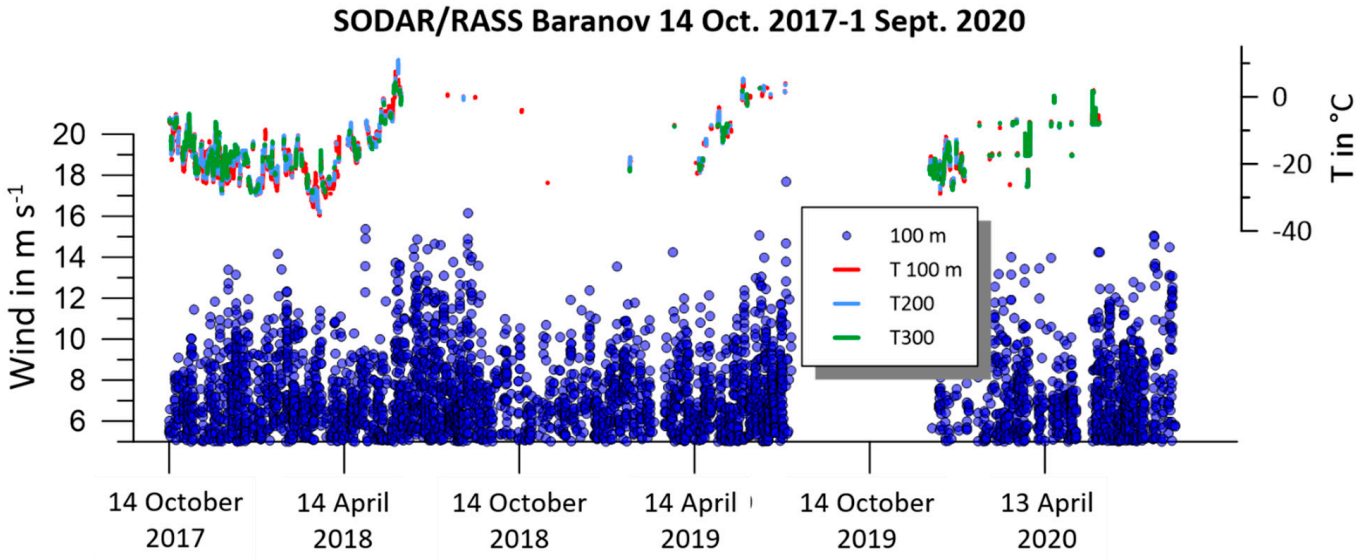

Figure 5. Hourly mean values of the SODAR wind speed at 100 m (blue dots) and RASS temperature at 100, 200 and 300 m (red, blue and green lines) for 1 October 2017–1 September 2020.

2.3. Numerical Model Data

The non-hydrostatic regional climate model Consortium for Small-Scale Model—Climate-Limited Area Mode (COSMO-CLM or CCLM, [21]) was used to produce a high-resolution atmospheric data set for the period October 2017 to August 2020. The model is nested in ERA5 data [15] and uses high-resolution sea ice concentration data [22] and sea ice thickness data [23] on a daily basis to keep the hindcast close to reality. The CCLM was adapted to the polar regions via the implementation of a thermodynamic sea ice model [6,24,25] and improved boundary layer parameterizations [26]. The model was run for the area of the Laptev and Kara Seas shown in Figure 1 with a resolution of 5 km. Apart from the region, the model setup was the same as in [6]. Topography data were taken from [27]. Full technical documentation of the CCLM model is given in [28]. No nudging was performed. In the vertical direction, the model extends up to 22 km with 60 vertical levels, 12 levels are below 500 m in order to obtain a high resolution of the boundary layer. The first model level is 5 m above the surface. Data is available every hour. Table 2 summarizes the CCLM configuration.

Table 2. Configuration of the CCLM simulations.

Forcing	Vertical/Horizontal Resolutions, Lowest Six Levels	Run Mode	Sea Ice Concentration (SIC) and Thickness
ERA5	60 levels, 5 km 5, 16, 31, 48, 70 and 96 m	Forecast mode (reinitialized at 18 UTC, 6 h spin-up)	AMSR2 PIOMAS

3. Verification of the CCLM for Near-Surface Variables

3.1. Statistics for the Comparison with Tower Data

Table 3 shows the statistics of the comparisons for the mean sea level pressure, 10 m wind and 2 m temperature data for the three years. We looked first at the comparison of the simulations for the grid point being closest to the observations (point Bc in Figure 2b). The simulated temperature showed a relatively large bias of −2.7 °C. The CCLM grid point was located over land at a distance of about 1 km from the coast, while the measurements were taken at a distance of about 100 m from the coast. This resulted in a larger amount of

cooling in the model on many days and also a too-large variability of the temperature, e.g., an overestimation of the daily temperature amplitude. As a measure of the daily amplitude (or more exactly, sub-daily temperature variability), an average daily amplitude (AA) was calculated by generating a low-pass filtered time series using a Gaussian filter with a filter width of 36 h, which was then subtracted from the original time series. This filtered time series contained only variations on the sub-daily scale. As a measure of the mean daily amplitude, the difference between the 90%- and 10%-tiles was calculated. This average amplitude was only shown for temperature and wind speed. For the temperature, the simulated average amplitude was larger by 1.4 °C compared with the observations. The filtered time series were also used for the calculation of correlations. The detrended correlation (Corr) of the whole temperature time series showed a very high value exceeding 0.96, which is a result regarding the good agreement in the seasonal cycle (see Figure 3). When only sub-daily variations were correlated (Corrsd), the correlation was only 0.66. In order to eliminate the seasonal cycle, a second low-pass filter with a width of 31 days was applied. The resulting correlation for the sub-monthly scale (Corrsm) was 0.87 for the temperature.

Table 3. Comparison of the CCLM at the grid point closest to the observatory (Bc) and for the closest grid point over the ocean (Bm) with near-surface observations (OBS) for 1 October 2017–31 August 2020 (2 m temperature (T), 10 m wind speed (wind) and mean sea level pressure (p). The average amplitude (AA) is the difference between the 90%- and 10%-tiles (after subtraction of the daily low-pass filtered time series, see text). RMSE—root-mean-square error, Corr—correlation after a linear detrend, Corrsd—correlation after applying a daily low-pass filter, Corrsm—correlation after applying a monthly low-pass filter. Diff AA is the difference AA(CCLM)-AA(OBS). The number of values was 25,561.

Quantity	OBS	CCLM	Bias	RMSE	Corr.	Corrsd	Corrsm	AA (OBS)	Diff AA (CCLM-OBS)
Closest Grid Point									
T in °C	−11.8	−14.5	−2.7	5.0	0.963	0.655	0.867	5.5	1.4
Wind in m/s	6.1	4.1	−2.0	3.2	0.839	0.749	0.835	7.5	−2.4
p in hPa	1011.6	1012.4	0.8	1.1	0.998	0.991	0.998		
Closest Grid Point Ocean									
T in °C	−11.8	−13.3	−1.5	3.6	0.962	0.634	0.859	5.5	0.3
Wind in m/s	6.1	5.3	−0.8	2.6	0.827	0.734	0.822	7.5	−1.4
p in hPa	1011.6	1012.4	0.8	1.1	0.998	0.991	0.998		

The wind speed was underestimated by the simulations by 2.0 m/s and also the AA was too low. Overall and sub-monthly scale correlations were similar (0.83) since there was no seasonal cycle, and it was 0.75 on the sub-daily scale. The pressure was simulated very well with a bias of 0.8 hPa and an RMSE of 1.1 hPa, and the correlations exceeded 0.99 on all time scales.

As stated above, the locations of the observations were at a distance of only 100 m from the coast such that is likely that there is a large influence of the marine environment on the measurements. Therefore a second comparison was made using the closest model grid point over the ocean (point Bm in Figure 2b). This led to a considerably smaller temperature bias, an improvement in the average amplitude and a smaller bias for the wind speed. It could be concluded that the simulations reproduced the observations relatively well, but the location of the tower was far from ideal and represented a mixture of land and marine influences.

3.2. Wind Distributions

The wind rose for the simulated 10 m wind at grid point Bc (Figure 6a) showed a good agreement with the observations (Figure 4a) with predominant southwesterly winds, but the peak in the wind direction was slightly more southerly and the winds larger than

10 m/s were underestimated. At grid point Bm (Figure 6b), the flow channeling was even more pronounced. The wind roses of the nine grid points around Baranova (see Supplementary Material Figure S5 for locations) are shown in Supplementary Material Figure S6. There was a tendency for more westerly winds over land grid points and more southerly winds over the ocean grid points.

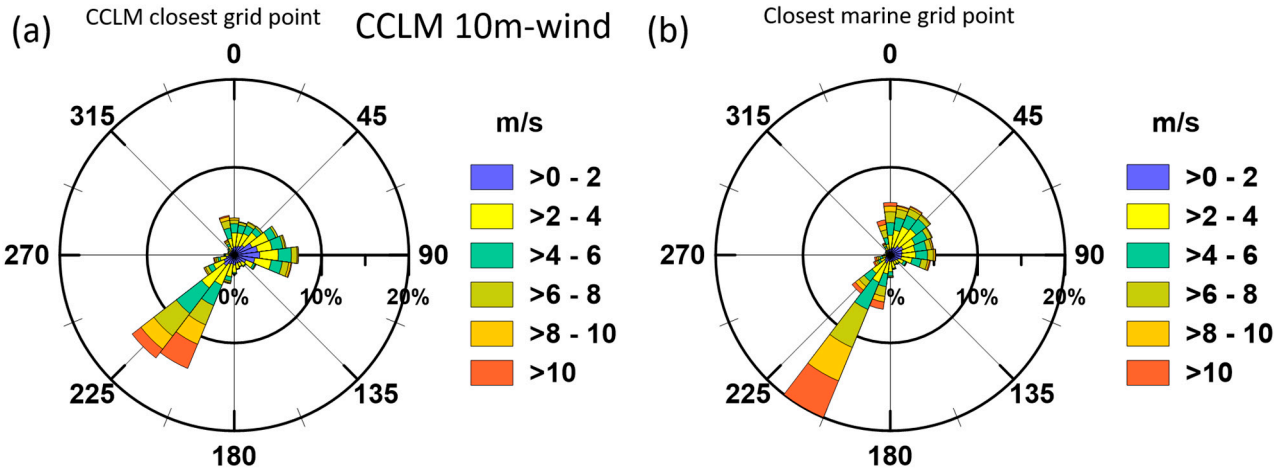

Figure 6. Wind roses (15° bins) for the 10 m wind for (**a**) grid point Bc and (**b**) grid point Bm for October 2017–August 2020.

4. Verification of the CCLM Using SODAR Data

4.1. Case Studies of Channeling Events

4.1.1. July 2018

During the period from 26 to 29 July 2018, an event of channeled flow occurred at Cape Baranova. Figure 7 shows the wind speed and wind direction at approximately 100 m in height from the SODAR data and CCLM simulations. The event on 27 July was associated with measured winds of 10–12 m/s and wind directions in the sector 205–245°, which agreed with the highest directional frequency found for the near-surface wind (see Figure 6). Before and after the event, the wind speed was low and from northerly directions. The simulations captured this event very well in general. There was an earlier onset and decay for the event, and the simulated maximum wind was smaller by 2–3 m/s. The change from northerly to channeled directions was captured very well by the simulations.

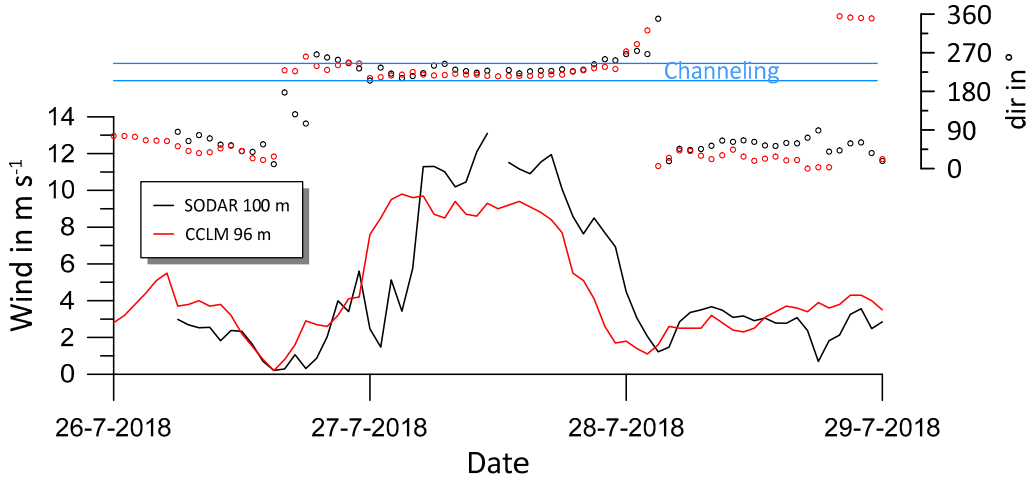

Figure 7. Wind speed (lower panel) and wind direction (upper panel) for 26 to 29 July 2018 for the SODAR measurements at about 100 m in height (black) and CCLM simulations at 96 m in height (time in UTC). The blue lines mark the sector characterizing channeled flow (205°–245°).

Time–height cross-sections of the wind speed for 26 to 29 July 2018 (Figure 8) showed the limitations of the SODAR data. While the data coverage was good below 100 m, the data gaps increased with increasing height, particularly for larger wind speeds. The SODAR data nicely monitored the channeling event but failed to resolve the vertical structure. The simulations showed this event as an LLJ with a core between 100 and 200 m, and in the sector of channeled flow (205°–245°). The simulations underestimated the wind speed, particularly below 100 m for this event.

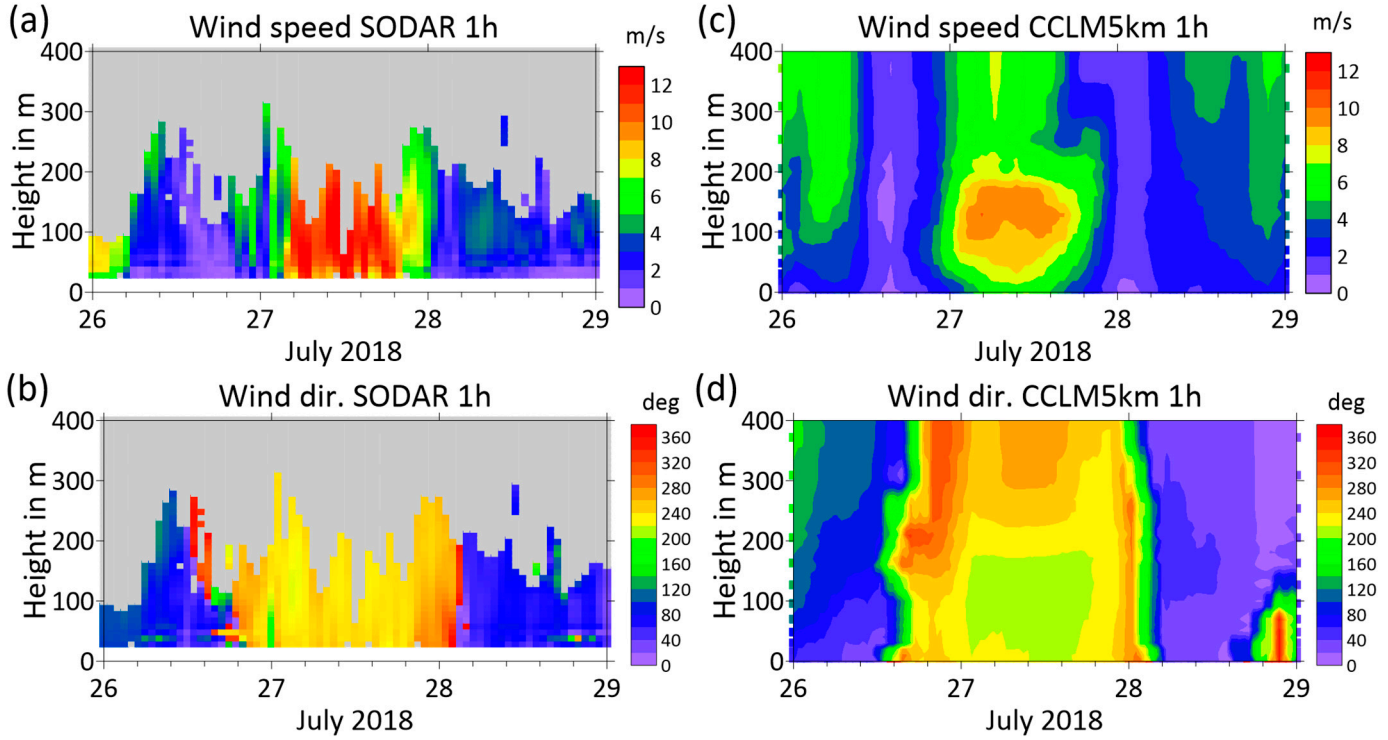

Figure 8. Time–height cross-sections of the wind speed and direction for 26 to 29 July 2018 for the SODAR data (**a**,**b**) and CCLM simulations (**c**,**d**). The CLLM data are shown as interpolated fields, SODAR data are shown as pixels (not interpolated) and missing data are grey.

Radiosondes were available for 0000 and 1200 UTC for this period since July 2018 was a YOPP special observation period with an increased frequency of radiosonde launches [3]. The sampling of 12 h was not sufficient to detect the channeling events and LLJs (Supplementary Material Figure S7). There was a weak signature of the channeling event in the radiosonde data at 1200 UTC on 27 July, but the vertical resolution was too coarse to resolve the LLJ. The comparison of the radiosonde data with the simulations for the lowest 600 m for the complete month of July 2018 showed that only a few LLJs were detected in the radiosonde data (Supplementary Material Figure S8), while the simulations showed frequent LLJs, which were associated with channeled flow in most cases (Supplementary Material Figure S9). The time resolution, as well as the problems of radiosonde wind measurements in the lowest 100 m, made it difficult to detect LLJs in operational radiosoundings [10,29,30]. It should be noted that measurements at Cape Baranova (synoptic data and radiosondes) were not used for the ERA5 reanalyses, which were used as initial and boundary conditions for the CCLM simulations.

The simulations of the 10 m wind field for the Shokalsky Strait area for the channeling event at 0600 UTC on 27 July (Figure 9a) showed that there was an inflow at the southern exit of Shokalsky Strait, which formed an elongated zone of increased winds in and at the northern exit of the strait, affecting the flow at CB. In addition to the channeling, the flow in the strait was affected by a gap flow between the main mountains on the eastern side of October Revolution Island. At a height of about 100 m (Figure 9b), the maximum

wind speed of 14 m/s was located southwest of CB and was about 2 m/s larger than the wind speed of the LLJ at CB. At a height of 200 m (Figure 9c), the wind field at CB was influenced not only by the channeled flow through the strait but also by the gap flow from October Revolution Island. The large-scale field of the mean sea level pressure for 0600 UTC on 27 July (Supplementary Material Figure S10a) showed a low east of Cape Baranova and a distinct pressure gradient at the southern tip of Bolshevik Island. At 850 hPa (Supplementary Material Figure S11a), a typically 4–6 m/s westerly to southwesterly flow was present for the whole area of the Archipelago Severnaya Zemlya.

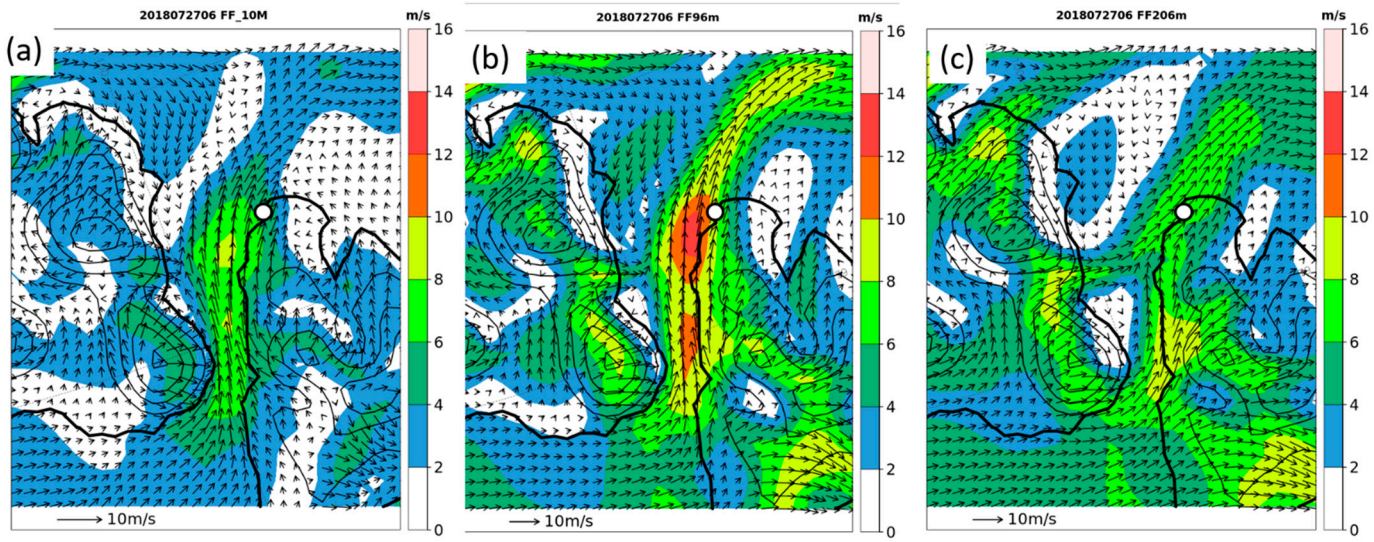

Figure 9. CCLM simulation results with a 5 km resolution of the wind speed (shaded, m/s) and wind vectors (scale at the bottom) for 27 July 2018, 0600 UTC for the area of Shokalsky Strait: (**a**) 10 m wind, (**b**) wind at 96 m and (**c**) wind at 206 m. The position of Cape Baranova is marked with a white circle, vectors are shown at every grid point and the topography is shown as isolines every 200 m.

4.1.2. April 2019

The second case study took place on 20 April 2019 under the influence of a cyclone with its center west of Komsomolets Island and a pronounced pressure gradient around Bolschevik Island (Supplementary Material Figure S10b). Winds at 850 hPa (Supplementary Material Figure S11b) showed the cyclone center over Komsomolets Island and an increase in wind speed with increasing distance from the center. Over October Revolution Island, the winds are very weak but increased toward Bolschevik Island, with a southwesterly flow at the southern exit of Shokalsky Strait. The wind field structure in the boundary layer (Figure 10) was similar to the case of July 2018, but the channeled flow was broader and more intense, and the downslope storm effect over Bolschevik Island due to stronger southwesterly winds could be seen (Figure 10a). Again, CB lay at the edge of the wind maximum at 200 m (Figure 10b). At a height of about 440 m, no wind maximum was present in the region of CB (Figure 10c).

The time–height cross-section of the simulated wind speed for this event (Figure 11a) showed an LLJ with a core between 100 and 400 m. The LLJ had a duration of about one day. Wind directions were in the sector of channeled flow (205°–245°) and showed a veering toward westerly directions with height. SODAR data indicated the wind direction change before and after the event at low levels (not shown), but the SODAR data were very scattered and there were no data during the main jet event.

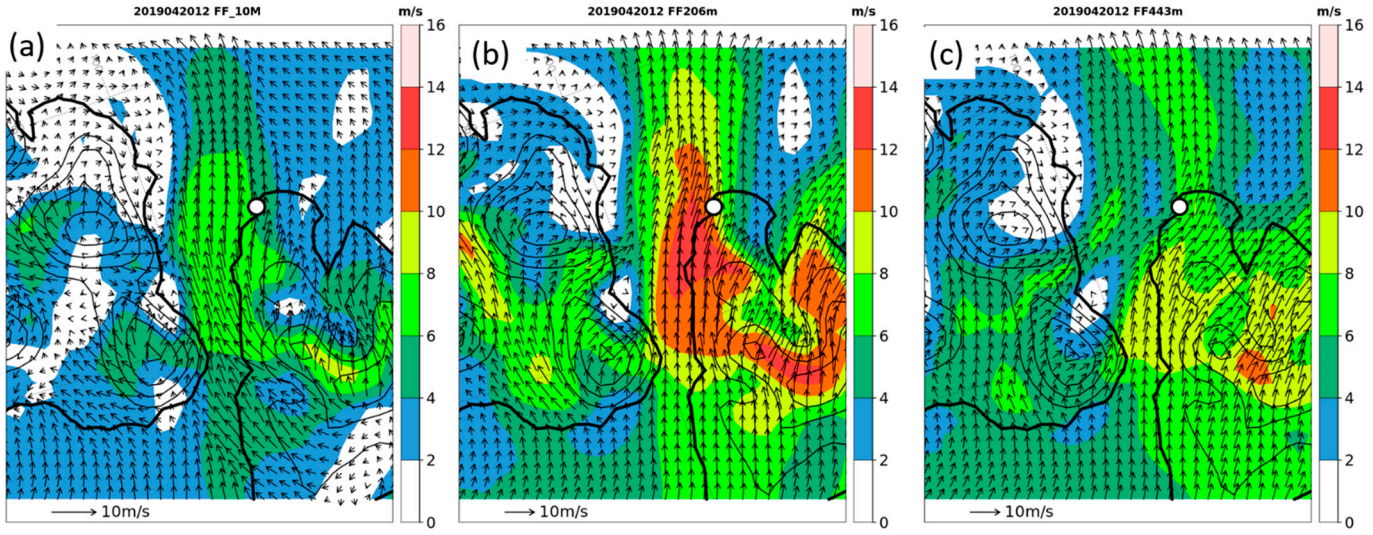

Figure 10. CCLM simulation results with a 5 km resolution of the wind speed (shaded, m/s) and wind vectors (scale at the bottom) for 20 April 2019, 1200 UTC, for the area of Shokalsky Strait: (**a**) 10 m wind, (**b**) wind at 206 m and (**c**) wind at 443 m. The position of Cape Baranova is marked with a white circle, vectors are shown at every grid point and the topography is shown as isolines every 200 m.

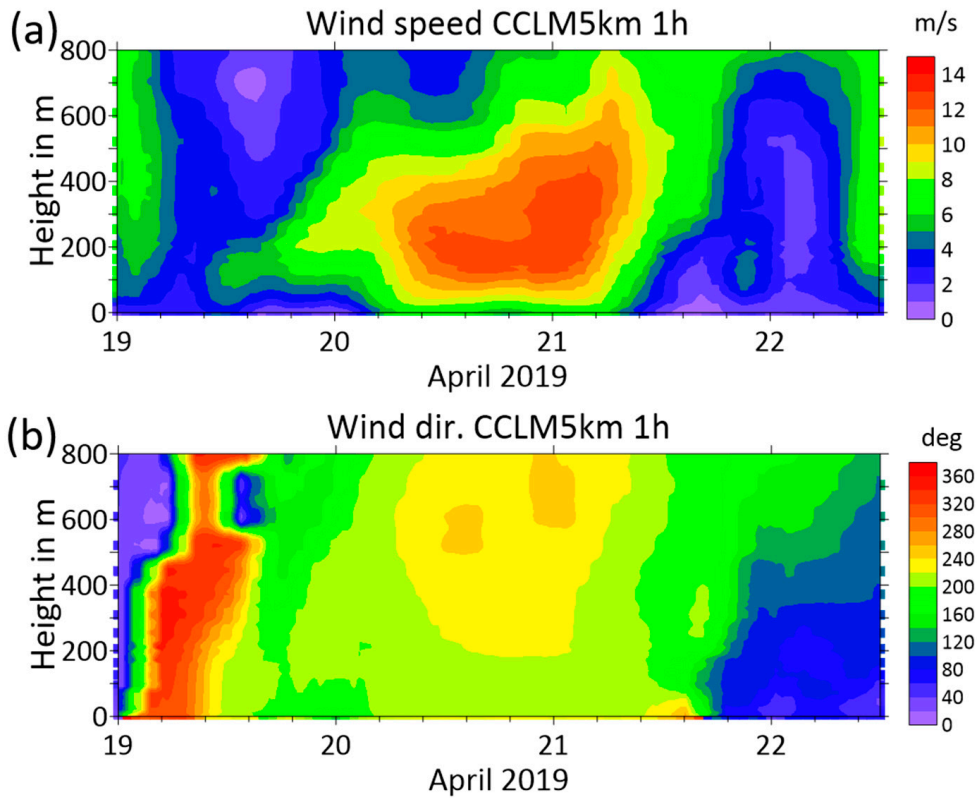

Figure 11. Time–height cross-sections of the wind speed (**a**) and direction (**b**) for 19 to 22 April 2019 for the CCLM simulations.

4.2. Statistics for the Comparison with SODAR Data

For the comparison of the simulations with SODAR data, only the CCLM data were used when SODAR data were available. The CCLM data were taken at the grid point Bc, which was close to the position of the SODAR. Figure 12 shows the results for the wind roses at 50 and 100 m. At a height of 50 m, the measured wind distribution (Figure 12a)

was similar to that of the 10 m wind (Figure 4), but with lower high wind speeds from the southwesterly sector. Part of the difference may result from the marine influence on the tower data (as discussed above), but there is also an underestimation of the frequency of winds exceeding 10 m/s due to the problems of the SODAR measurements. As stated in Section 2.2, the availability of SODAR data at 50 m was only 52%. The simulations at the times of the SODAR data at 50 m (exact model level was 48 m) showed the southwesterly directions with a higher frequency compared with the SODAR data (Figure 12b). These differences get larger at 100 m (exact model level was 96 m), where the simulations also showed wind speeds higher than 10 m/s with a higher frequency.

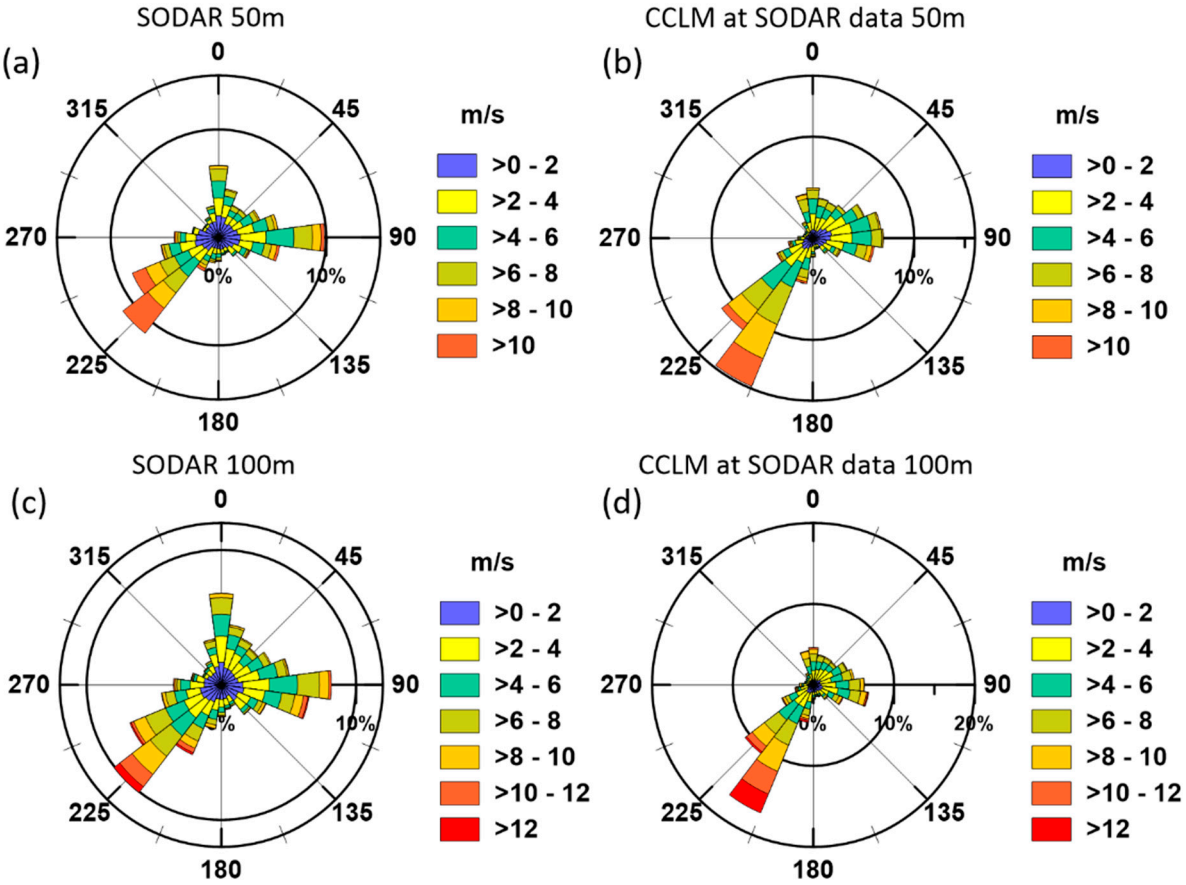

Figure 12. Wind roses (15° bins) for the SODAR wind at 50 m (**a**) and 100 m (**c**) and the CCLM simulations at the times of available SODAR data at 50 m (**b**) and 100 m (**d**) based on 1 h values for October 2017–August 2020.

The statistics of the comparisons for the wind speed at different heights are shown in Figure 13a. At 50 m in height, there was a small positive bias of 0.6 m/s, which increased to 1.5 m/s at larger heights. At the same time, the number of available SODAR data decreased significantly with height. The number of hourly CCLM data was 25,585, that is, only 28% and 15% of the data could be compared for heights of 200 and 300 m, respectively. This undersampling was demonstrated in Figure 13c for the wind simulations at 100 m. The undersampling was present at all wind speeds but increased for speeds exceeding 6 m/s. Wind speeds with 16 m/s and more were missed completely when taking only data at times of available SODAR data. The wind speeds sampled at the times of the SODAR data did not represent the wind distributions, particularly at larger heights (Supplementary Material Figure S12). The comparison of the wind speed distributions for available SODAR data at 100 m (Figure 13b) showed the overestimation of the wind speed in the simulations starts with speeds of 6 m/s. This was even more pronounced for larger

heights (Supplementary Material Figure S13). Therefore, complete statistics of the wind in the ABL for the three years period could only be obtained via the simulations.

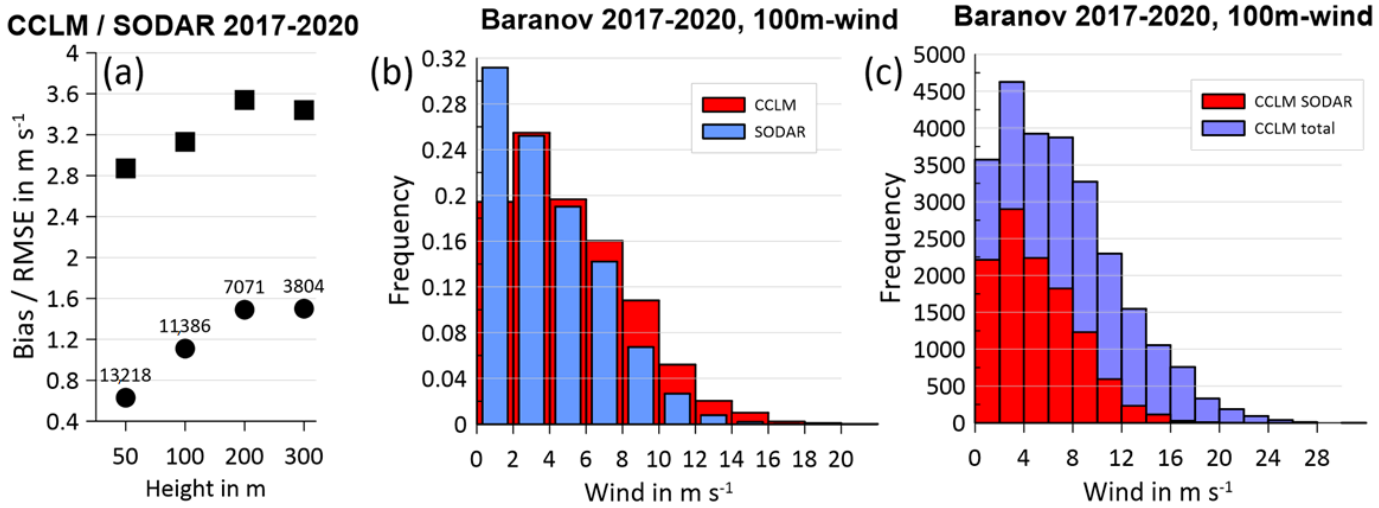

Figure 13. (**a**) Bias (CCLM-SODAR, dots) and RMSE (squares) for the comparison of the wind speed from the SODAR and CCLM simulations at different heights (numbers of data points as labels). (**b**) Wind speed distributions of SODAR and simulations at the times of available SODAR data at 100 m (relative frequencies). (**c**) Wind speed distributions at 100 m for the CCLM data at the times of available SODAR data and for all the CCLM data (absolute frequencies). All statistics were based on 1 h values for October 2017–August 2020.

5. Wind Climatology

5.1. Climatology of Channeling Events

The following climatology of wind statistics and channeling events was completely based on the simulations with a 1 h resolution for the three years. The channeling effect with the highest frequency of wind directions in the sector of 205 to 245° was clearly visible in the low-level wind statistics. This prevailed for 200 and 300 m in height (Figure 14a,b), but at 300 m in height, the distribution became broader. At 600 m in height (Figure 14c), the channeling effect was no longer present, which was in agreement with the topography of Schokalsky Strait.

If only strong winds $\geq$ 15 m/s were considered, the wind distributions at 200 and 300 m in height (Figure 14d,e) showed almost exclusively the wind channeling. At 600 m in height (Figure 14f), almost all high winds occurred during southerly to westerly synoptic flows.

A climatology of channeling events was determined at different heights by selecting all simulation times with wind directions in the sector from 205 to 245°. All consecutive hours fulfilling this criterion were counted as one event. If the time difference between the end of one event and the start of the next event was less than 2.5 h, the two events were considered to be the same event. The following evaluations are shown for 200 m in height, which was the typical height of the wind maximum (see case studies). Overall, 618 events were detected over the three years. The mean duration of the events was 12.2 h, the maximum duration was 137 h and the 75%-tile was 16.0 h. The distribution of the maximum wind during the events is shown in Figure 15a for all events. The mean wind speed was 9.7 m/s and the 75%-tile was 14.4 m/s. The highest wind speed was 34.4 m/s. The distribution changed if we considered only events with a duration $\geq$ 12 h (Figure 15b). Here, we saw the highest frequencies in the range of 14–20 m/s (mean 16.6 m/s) and the 75%-tile was 20.1 m/s. Thus, the long events were associated with generally higher wind speeds. The channeling events were mainly driven by the synoptic situation, and there was no indication of a diurnal cycle.

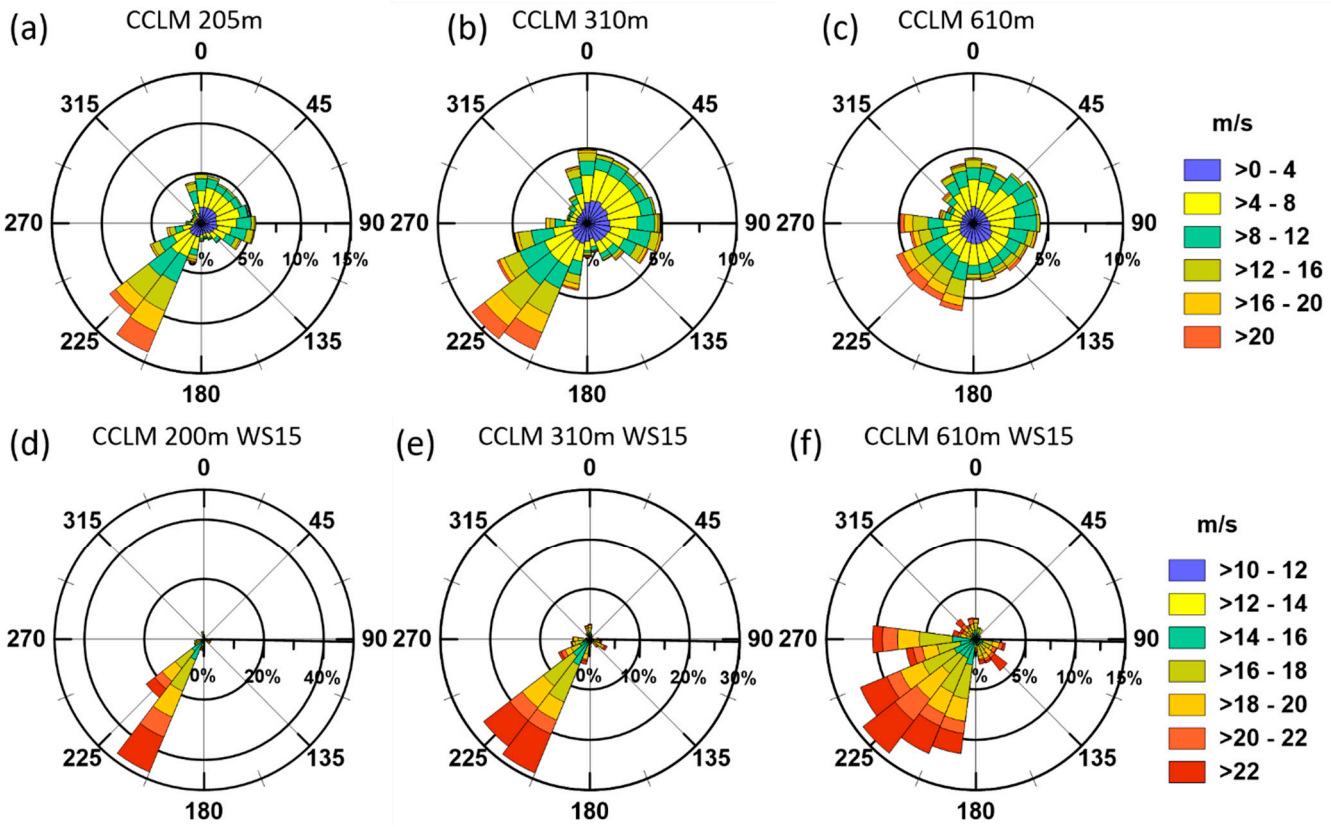

Figure 14. Wind roses (15° bins) from the CCLM simulations at 205, 310 and 610 m based on 1 h values for October 2017–August 2020: (**a**–**c**) all data and (**d**–**f**) only for wind speeds ≥ 15 m/s.

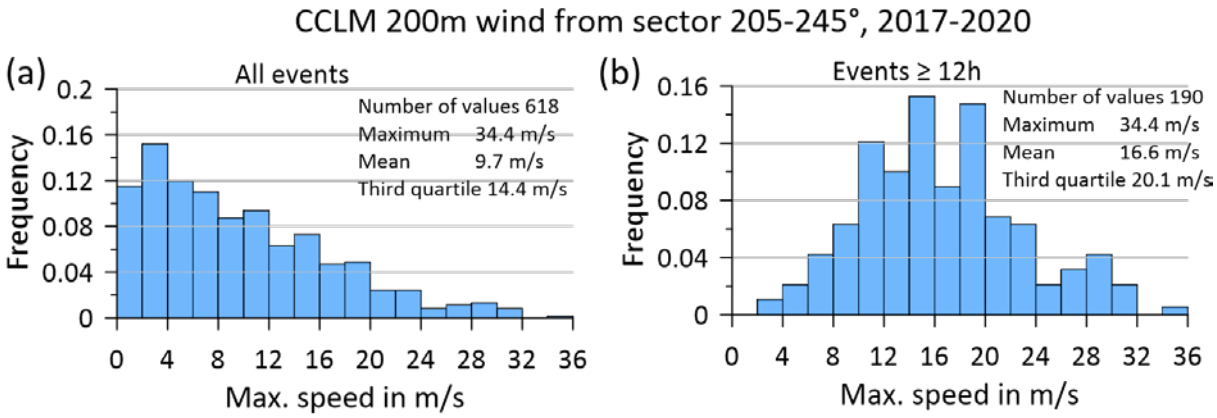

Figure 15. Distributions of the maximum wind speed for channeling events at 200 m in height from the CCLM simulations for October 2017–August 2020: (**a**) all events and (**b**) only for events with a duration ≥ 12 h.

So far, we have only evaluated the conditions in the vicinity of Cape Baranova. In order to study the flow conditions in the complete Shokalsky Strait, additional grid points were selected for the analysis (see Figure 2b): grid point Sn (Shokalsky north) at the northern exit of the strait, grid point Ss (Shokalsky south) at the southern exit of the strait and grid point Sw (Shokalsky west) in the middle of the strait at the western side. Sw lay in the region where the gap flow through the mountains of October Revolution Island was found in the case studies. Figure 16 shows the wind distributions at these three grid points for the 10 m wind and the wind at 100 m in height, with the latter only for strong winds (wind speeds ≥ 15 m/s). At Sn (Figure 16c), we found a distribution similar to the marine grid

point close to Cape Baranova, but with less frequent easterly directions such that the wind direction distribution was more or less bimodal along the axis of the strait with the highest wind from the south-southwest. At the southern end of the strait (Figure 16a), the flow conditions were reversed: here, the main wind direction with the strongest winds was from the northeast. In the middle of the strait (at Sw, Figure 16b), the combined effect of channeled winds from the northern and southern exits of the strait can be seen. There was a tendency toward more frequent strong wind from the south. This finding was clearly shown for strong winds at 100 m in height (Figure 16e), which were predominant from the south. An interesting detail was the second maximum of strong winds from westerly directions, which were associated with the gap flow from October Revolution Island and were present in about 20% of the strong wind cases. For the grid points Sn and Ss, strong winds at 100 m were dominated by the channeling effect.

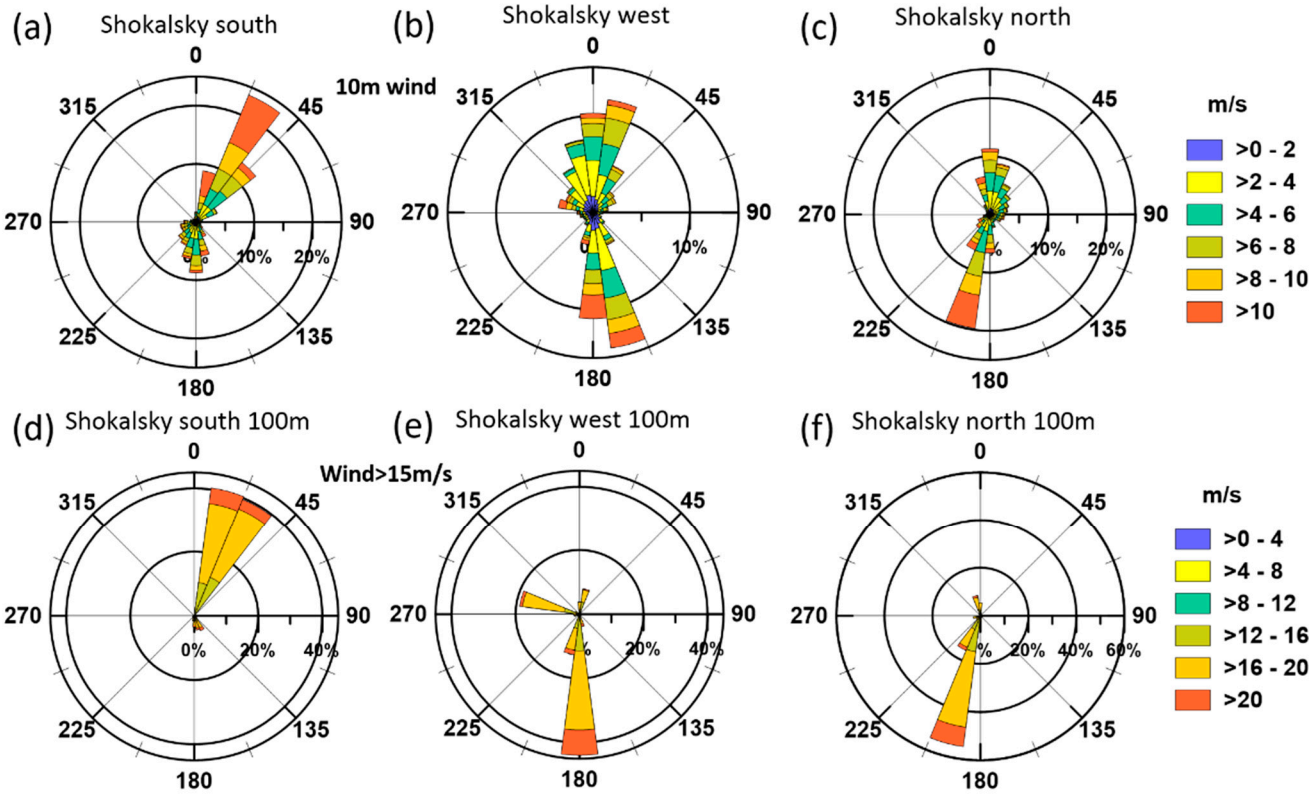

Figure 16. Wind roses (15° bins) for October 2017–August 2020 at the grid points Shokalsky south, Shokalsky west and Shokalsky north (see Figure 2b for locations) for the 10 m wind (**a**–**c**) and the wind at 100 m for wind speeds $\geq$ 15 m/s (**d**–**f**).

Channeled flows are ageostrophic and driven by the pressure gradient along the channel [13,17]. Therefore we looked at the pressure difference between the grid points Ss and Sn and related this difference to the flow component along the strait and at both points. Figure 17 shows the result for the 10 m wind at grid points Ss and Sn. The wind speed component along the strait (vrel) was computed relative to a direction of 205°. Thus, a positive vrel corresponded to an outflow at the northern exit of the strait, and a negative vrel corresponded to an inflow at the northern exit of the strait. At the southern exit, this was just reversed.

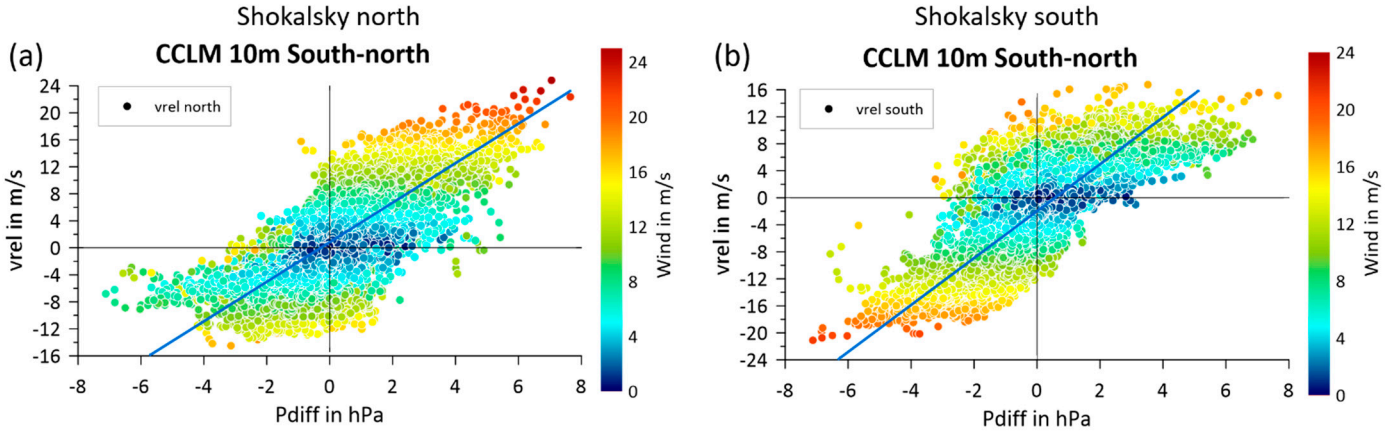

Figure 17. Mean sea level pressure difference (Ss-Sn, hourly values) for October 2017–August 2020 versus the 10 m wind component along the strait (vrel) at the grid points Shokalsky north (**a**) and Shokalsky south (**b**). The color code indicates the 10 m wind speed. Lines are the linear regressions using all data.

At the northern exit (Figure 17a), the outflow was related to a positive pressure difference, that is, a higher pressure at the southern entrance of the strait. The distance between the grid points Sn and Ss was about 80 km. Due to the channeling, the outflow component was almost as large as the 10 m wind speed. For inflow conditions at Sn (negative vrel), there was only a weak dependence of the inflow to the pressure difference. At Ss, conditions were reversed (Figure 17b). Here, the highest outflow speeds (negative vrel) were associated with a negative pressure difference, that is, higher pressure at Sn. Again, the outflow component was almost as large as the 10 m wind speed. Inflow conditions at Ss (positive vrel) were associated with larger wind speeds and a larger scatter for high wind speeds, which may have been caused by flow around the southern part of October Revolution Island (see Figure 9a).

5.2. Climatology of LLJs

The case studies already showed good examples of LLJs associated with channeling. The analysis of LLJs follows the method used in [30]. The lowest wind maximum was searched for below 1000 m, then the next minimum above the maximum was searched for below 1500 m, but limited by a search radius of 1.5 times the height of the maximum. Then, an absolute criterion of at least 2 m/s difference between the wind maximum and minimum was required. This LLJ detection was performed for the CCLM grid point Bc at Cape Baranova with an hourly resolution for the whole period.

Overall, the LLJs were detected in 37% of all profiles. The highest frequencies for the jet height (Figure 18a) were found between 50 and 250 m. The average jet height was 247 m, and the 25% and 75%-tiles were 127 and 309 m, respectively. The jet speed (Figure 18b) had a mean of 12.6 m/s and 25% and 75%-tiles of 8.5 and 15.9 m/s, respectively. As expected, most LLJs were associated with channeling, but a secondary maximum existed for easterly directions (Figure 18c). The directional shear between the wind at the LLJ height and the lowest model level (5 m) was generally small with a slight bias to positive values (Figure 18d). The statistics for strong LLJs (jet speed $\geq$ 15 m/s) were similar to Figure 18 (Supplementary Material Figure S14), where the main differences were fewer LLJs below 150 m and fewer LLJs from easterly directions.

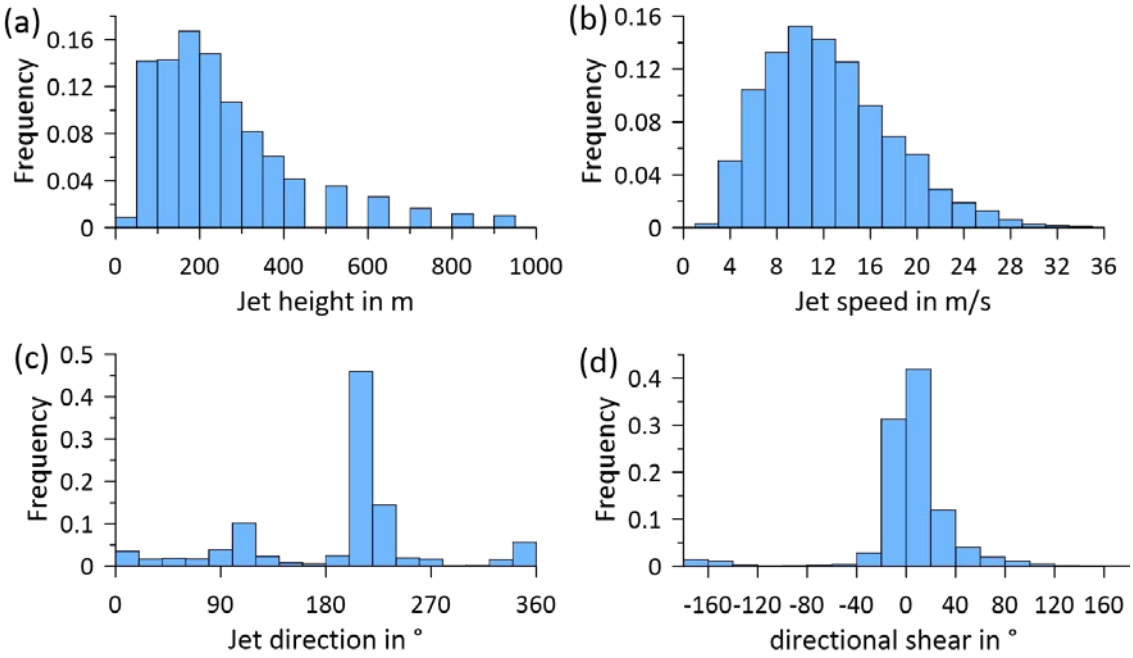

Figure 18. Statistics (relative frequencies) for LLJs from the CCLM simulations at Cape Baranova of the (**a**) jet height, (**b**) jet speed, (**c**) jet direction and (**d**) directional shear (difference between the wind direction at the jet core and at a height of 5 m).

The directional shear (Figure 18d) was consistent with a shear due to friction, but for the channeled flow, this was likely caused by synoptic conditions. This was also demonstrated by the average LLJ profiles for the lowest 1200 m (Figure 19). The mean wind profile (Figure 19a) showed a pronounced maximum at about 150 m (note that the height of the mean wind speed maximum was not the same as the mean LLJ height). Although the directional shear was relatively small between the wind maximum and the lowest level, there was a shear from about 210° at the LLJ height to 250° in the synoptic flow (Figure 19b). The mean stability was described by the average of the potential temperature anomaly in the lowest 2000 m for each level and for each profile. This corresponded to the concept of a temperature deficit often used for polar boundary layer studies. It shows the stable stratification for the LLJs with an increase of the potential temperature by 8 °C in the lowest 600 m (Figure 19c).

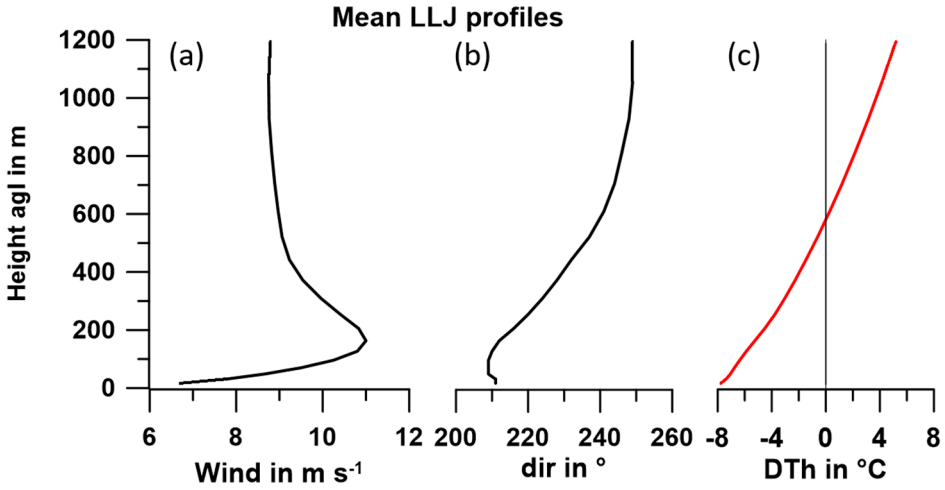

Figure 19. Mean vertical profiles for all LLJs of the wind speed (**a**), wind direction (**b**) and potential temperature deviation (**c**) (see text).

A more detailed analysis of the LLJ wind profiles is shown in Figure 20. We focused on strong jets. Since the 75%-tiles of LLJ speed distribution was 15.9 m/s, we defined strong LLJs as jets with a jet speed $\geq$ 15 m/s (which were 29% of all LLJs). The mean wind maximum for strong LLJs was again at about 150 m (Figure 20a), but the wind anomaly was less pronounced than for the mean of all LLJs. This was a result of the variability in LLJ height. The jet structure was clearer if only strong LLJs with heights $\leq$ 300 m were considered (Figure 20b). The restriction to 300 m was chosen because it roughly matched the 75%-tile of the LLJ height distribution (see above). Channeled LLJs were present in 58% of all cases and with a fraction of 73% for strong jets. This means that most strong jets were associated with channeling events. The mean wind profile of strong channeled jets (Figure 20c) was similar to that of low strong jets.

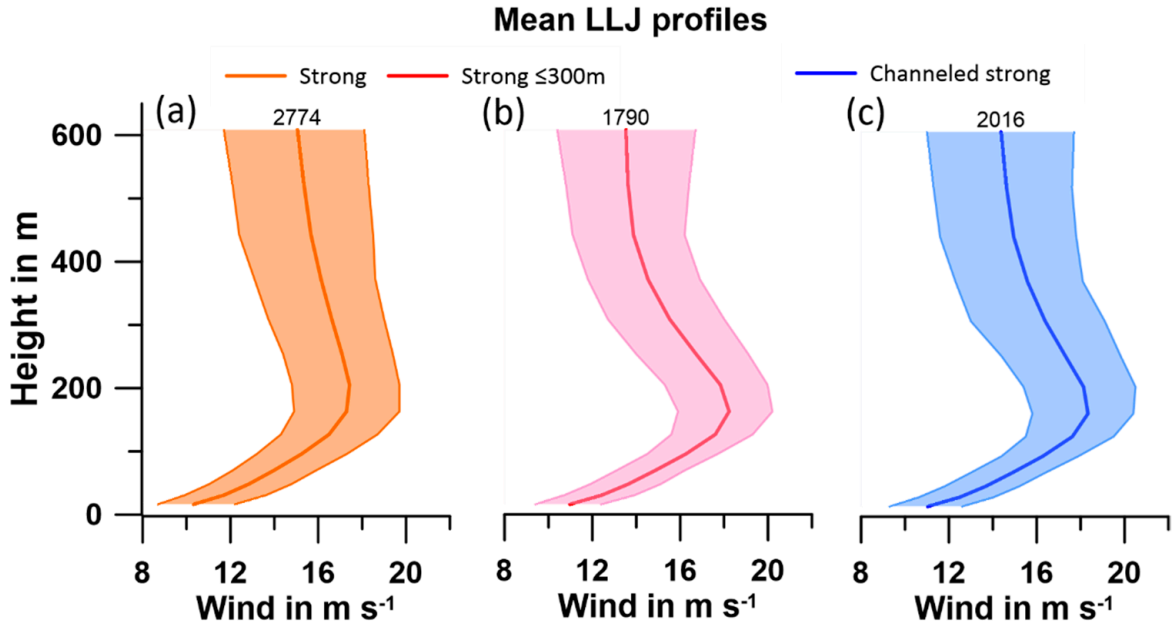

Figure 20. Mean vertical profiles of the wind speed for (**a**) strong LLJs, (**b**) strong LLJs below 300 m in height and (**c**) strong channeled LLJs. Strong—jet speed $\geq$ 15 m/s, labels indicate the number of profiles. The shaded regions mark the 25%- and 75%-tiles, respectively.

Flow channeling requires a stable stratification of the ABL, which is given for the LLJs (Figure 19), but also a blocking by the mountains in the entrance region of the strait. This can be expressed by the mountain Froude number Fr_m [12]:

$$Fr_m^2 = \frac{U_m^2}{\frac{g}{\theta_m}\Delta\theta_m \cdot h_m} \quad (1)$$

The mountain height h_m was taken as 700 m for Shokalsky Strait. The mean wind speed U_m, the mean potential temperature θ_m and the bulk difference of the potential temperature $\Delta\theta_m$ between h_m and the lowest model level were calculated for grid point Ss, which represented the entrance region for channeled LLJs at Cape Baranova (see Figure 2b). The statistics of the upstream mountain Froude number (Figure 21a) for channeled LLJs showed that Fr_m was smaller than 1 in almost all cases. The mean was 0.56 and the 75%-tile was 0.68.

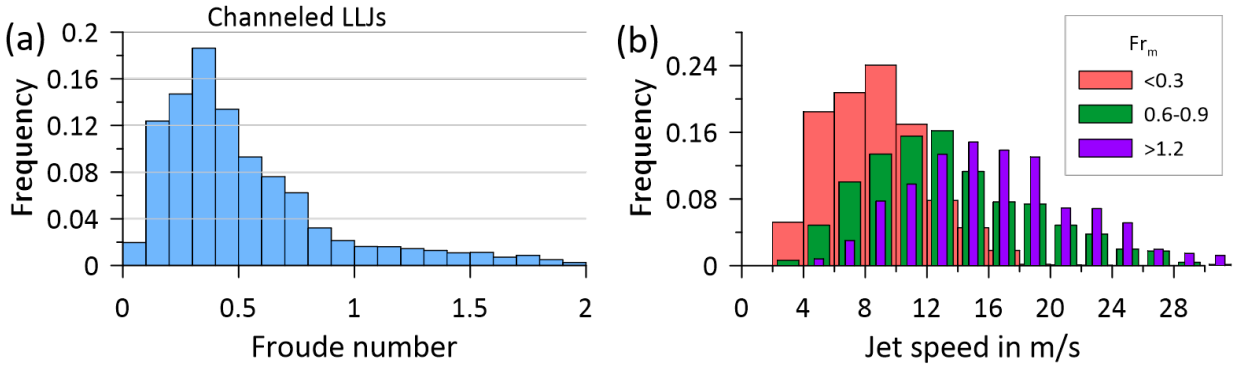

Figure 21. Statistics (relative frequencies) for channeled LLJs from the CCLM simulations at Cape Baranova: (**a**) upstream mountain Froude number and (**b**) LLJ speeds for different mountain Froude number classes.

The upstream mountain Froude number also influences the LLJ speed distribution (Figure 21b). The maximum of the speed distribution became larger with increasing Fr_m. The same held for the LLJ height (Supplementary Material Figure S15).

5.3. Mean Wind Field and Extremes

The CCLM simulations were used for the wind climatology for the area of Shokalsky Strait for 2017–2020. The field of the mean 10 m wind (Figure 22a) showed the presence of a channeled flow in Shokalsky Strait with larger winds at the southern exit. The wind field over the islands was dominated by downslope winds. The mean wind speed was 5–6 m/s in the northern part and 6–7 m/s in the southern part of the strait. Note that the vector mean speed was smaller than the mean speed, indicating the variability of the wind direction. In contrast to the case studies shown in Section 4.1, which were selected because of the observations at Cape Baranov, the field of the mean 10 m wind vectors showed that channeling occurred at both exits of Shokalsky Strait. Since the inflow was associated with lower wind speeds than the outflow, the mean wind field reflected the dominating outflow at both exit regions.

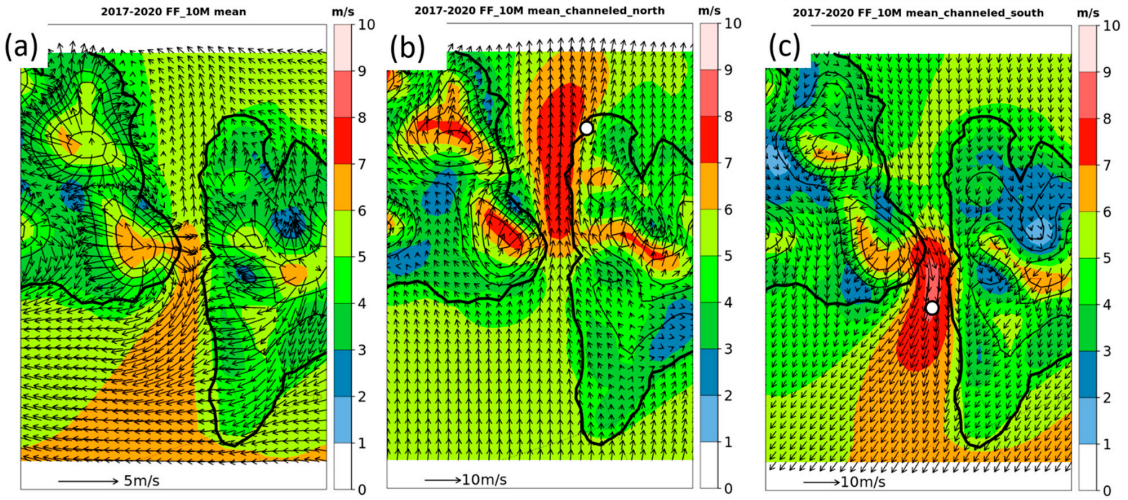

Figure 22. Simulated 10 m wind speed (shaded) and mean wind vectors (scale at the bottom) for the area of Shokalsky Strait for 2017–2020. (**a**) Mean wind for the period October 2017–August 2020 based on hourly values; (**b**) mean wind for days with channeling events with a duration $\geq$ 12 h at 200 m in height at Cape Baranova (marked by a white circle, 190 days in total); (**c**) mean wind for days with channeling events with a duration $\geq$ 12 h at 200 m in height at grid point Shokalsky south (marked by a white circle, 193 days in total). Vectors are shown at every grid point and the topography is shown as isolines every 200 m.

The channeling process at both exit regions could be clearly seen if we took composites of the flow during channeling events. This was done by averaging all days when channeling events occurred with a duration $\geq$ 12 h at 200 m in height. The flow field for channeling events at Cape Baranova (Figure 22b) showed a similar structure as for the case studies. The flow entered Shokalsky Strait from the south and accelerated in the strait, where the confluence was supported by the downslope winds of the islands. The influence of the gap flow from October Revolution Island on the wind field at Cape Baranova, as found in the case studies, could also be seen in the composite of channeling events (Figure 22b), but it was not present in the climatological mean (Figure 22a). The flow field for channeling events at the Shokalsky south grid point (Figure 22c) showed a reversed situation. This was in agreement with the field of the mean sea level pressure for channeling events (Supplementary Material Figure S16). For channeling events at Cape Baranova (Supplementary Material Figure S16a), there was a low over the northeastern Kara Sea and a high over the southern Laptev Sea, which resulted in a distinct pressure gradient in the region of Shokalsky Strait associated with a southwesterly flow. For channeling events at the Shokalsky south grid point (Supplementary Material Figure S16b), the mean pressure field showed a low over the southwestern Laptev Sea and high pressure over the northeastern Kara Sea, which resulted in a northeasterly flow in the region of the Archipelago Severnaya Zemlya.

The channeling effect was also present when we looked at the extremes. Figure 23a shows the 99%-tile of the wind speed for the whole period, which reached 18 m/s and clearly showed the dipole structure of channeled wind at both exits of the strait. In order to reflect the wind field structure for strong winds, the mean wind vectors for wind speeds $\geq$ 10 m/s at each grid point are shown (based on hourly values). The seasonality of the wind extremes is shown for December–February and June–August (average of all months) in Figure 23b,c. During the core winter season, extreme winds were stronger in the northern part of Shokalsky Strait than in the southern part (Figure 23b). In summer, it was the other way round, but extreme winds were weaker compared with winter (Figure 23c). For March–May (Supplementary Material Figure S17a), extremes showed a dipole structure similar to the annual mean, while for September–November (Supplementary Material Figure S17b), the structure was less clear.

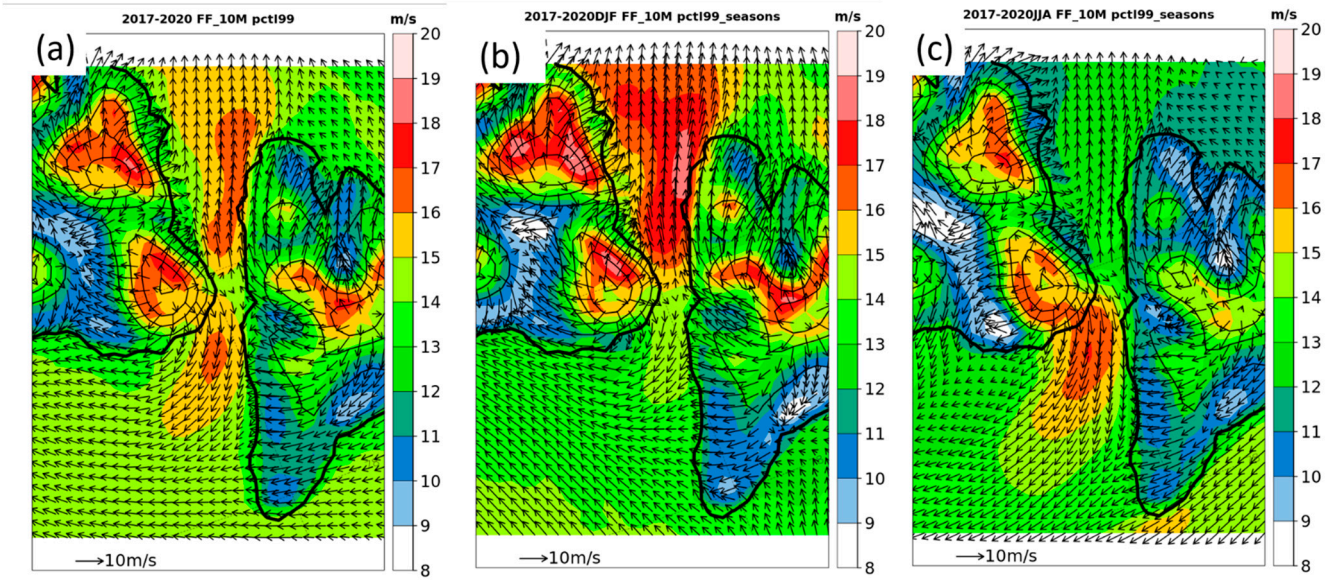

Figure 23. Simulated 99%-tile of the 10 m wind speed (shaded) and mean wind vectors for speeds exceeding 10 m/s based on hourly values for the area of Shokalsky Strait for 2017–2020. (**a**) For the period October 2017–August 2020, (**b**) December–February and (**c**) June–August. Vectors are shown at every grid point and the topography is shown as isolines every 200 m.

6. Discussion

In the present study, SODAR measurements of the ABL were performed for three years during the YOPP period at Cape Baranova in the Archipelago Severnaya Zemlya of the Siberian Arctic. In addition, simulations using the regional climate model CCLM in forecast mode at a horizontal resolution of 5 km were performed. Since Cape Baranova is located at the northern end of the Shokalsky Strait in a topographically structured area, the foci of this study were the topographic flows and LLJs.

The observations at Cape Baranova were used for verification of the CCLM simulations. The comparison with near-surface measurements showed biases of −2.0 m/s and −2.7 °C for the 10 m wind and the 2 m temperature, respectively. These differences were larger than the results of other verification studies for the CCLM [6,25,26,29,31]. A comparison of the CCLM with resolutions of 3 and 13 km with coastal stations in the Kara Sea for four months yielded mean wind biases in the range of ±0.5 m/s [32], but they also reported large errors for a station affected by strong downslope winds. Ref. [17] compared the CCLM simulations for 1987–2017 with meteorological stations in the area of Nares Strait. They found wind speed biases in the range of −1.5 to 0.9 m/s and temperature biases in the range of 0.5 to −5.7 °C for the winter, which resulted from the fact that the observations were taken at stations close to the coast and the observations were influenced by local effects. Comparisons with near-surface measurements at Cape Baranova were also problematic since the location of the observations was at a distance of only 100 m from the coast. The comparison of the simulations with the closest model grid point over the ocean yielded reduced biases (−0.8 m/s and −1.5 °C).

The SODAR data showed limitations with respect to the vertical range, particularly for high wind speeds. The same problem was present for SODAR measurements made by [10] for one year at Tiksi (Figure 1), but this problem was found to be much larger at Cape Baranova. Taking the available SODAR wind profiles for the verification of the CCLM, we found a small positive bias of 0.6 m/s at 50 m in height, which increased to 1.5 m/s at larger heights. Particularly, wind speeds larger than 8 m/s were overestimated by the CCLM. The errors of this overestimation seem to be small compared with the errors due to the undersampling of the SODAR data. The wind speeds sampled at the times of the SODAR data did not represent the wind distributions in the ABL, which were dominated by the channeling in Shokalsky Strait. This channeling was associated with LLJs in most cases. Thus, the climatological analyses of LLJs and channeled flow were mainly based on the simulations.

There were only a few long-term observational or model studies of ABL structures for high latitudes. Ref. [10] analyzed SODAR data with respect to LLJs for the winter period of 2014/15. They found that in about 23% of all profiles, LLJs were present with a mean jet speed and height of approximately 7 m/s and 240 m, respectively. LLJs with speeds exceeding 10 m/s occurred in 3.4% of all profiles. In the present study, LLJs were detected more frequently (in 37% of all profiles) and with a much higher mean speed of 12.6 m/s. A total of 29% of the LLJs exceeded 15 m/s (corresponding to 11% of all profiles).

The channeling and associated LLJs in Shokalsky Strait were not reflected by the pan-Arctic climatology of LLJs for 2000–2010 by [11], which was caused by the relatively coarse resolution of their data (30 km). The study of [16] with a 15 km resolution for 1979–2016 showed only a weak signal of flow channeling in Shokalsky Strait for the 95%-tile of the 10 m wind. Radarsat-2 satellite data in the study of [33] showed an example of channeling for the northern exit of Shokalsky Strait, with maximum wind speeds of about 10 m/s, and the wind field structure resembled our findings for the case studies and the climatology. Our results showed a clear dipole structure of the climatological wind field due to the channeling at both exits of Shokalsky Strait. We found more events for channeling at the northern exit (about 200 per year) than for the southern exit (about 145 per year), but channeling events lasting at least 12 h occurred with the same frequency for both regions (on about 62 days per year). The climatology of channeling events lasting at least 12 h showed pronounced channeling during northeasterly flow at the southern exit and

during southwesterly flow at the northern exit. The 99%-tile of the 10 m wind showed that channeling of the southerly flow through the strait was most pronounced during winter with wind speeds exceeding 18 m/s, while channeling during northerly flow through the strait was stronger during summer.

The channeling was driven by the pressure difference between the northern and southern exits of the strait. The pressure differences were 6–8 hPa for the strongest cases of channeled flow with 10 m wind speeds of more than 20 m/s. For the Smith Sound of Nares Strait, [17] found pressure differences of more than 20 hPa along the strait associated with 10 m wind speeds of more than 25 m/s. The main part of the pressure differences was visible between the entrance and exit region of Smith Sound, while the wind maximum was located downstream of the gap. A gap flow situation similar to Shokalsky Strait was found also in the Hindelopen Strait at Svalbard [34,35]. It was argued by [35] that the tip jet effect [36] at the northeastern tip of the main island Spitsbergen was responsible for the extension of the wind maximum downstream of the gap. This additional amplification and extension of the area of the wind maximum seemed to be present also in Shokalsky Strait.

The channeling in Shokalsky Strait was analyzed in the framework of the mountain Froude number (Fr_m) following the concept of [37]. Channeled LLJs at Cape Baranova were mainly present for upstream $Fr_m < 1$, that is, the flow was too weak to flow over the mountains. As in [17], we also found an increase in the jet speed and height with increasing Fr_m.

As an interesting feature, we found that the westerly gap flow between the mountains of October Revolution Island also played a role in the wind conditions at Cape Baranova. For wind speeds exceeding 15 m/s, we found that this gap flow was present in about 20% of the strong wind cases in the middle part of the strait.

7. Conclusions

This study gave new insights into the flow conditions for an area with complex topography in the Laptev Sea area using unprecedented ABL measurements and high-resolution simulations for this region. When using data from Cape Baranova (near-surface measurements, radiosondes), it should be kept in mind that these measurements are largely influenced by the local topography for the lowest 600 m, which requires resolutions of at least 5 km to be represented in reanalyses, weather forecasts and climate models. A full picture of the ABL climatology in this region can be obtained only with model data. A dedicated experiment with high-resolution wind and temperature profiles on both sides of Shokalsky Strait would be a vision for the future.

Supplementary Materials: The following supporting information can be downloaded from https://www.mdpi.com/article/10.3390/atmos13060957/s1. Figure S1: Research Station "Ice Base Cape Baranova" and its surroundings from a height of 200 m; Figure S2: Meteorological station at Cape Baranova; Figure S3: The phased-array antenna of the SODAR and the SODAR/RASS installation; Figure S4: Profiles of the availability of SODAR data; Figure S5: Location of the CCLM grid points in the vicinity of Cape Baranova; Figure S6: Wind roses for the 10 m wind at the CCLM grid points in the vicinity of Cape Baranova; Figure S7: Time–height cross-sections of the wind speed and direction for 26 to 29 July 2018 for radiosonde data; Figure S8: Time–height cross-sections of the wind speed and direction for July 2018 for radiosonde data; Figure S9: Time–height cross-sections of the wind speed and direction for July 2018 for the CCLM simulations; Figure S10: CCLM simulations with 5 km resolution of the mean sea level pressure and 10 m wind speed for the area of the Kara and Laptev Sea for (a) 27 July 2018, 0600 UTC, and (b) 20 April 2019, 1200 UTC; Figure S11: CCLM simulations with a 5 km resolution of the wind field at 850 hPa for the area of the Severnaya Zemlya Archipelago for (a) 27 July 2018, 0600 UTC, and (b) 20 April 2019, 1200 UTC; Figure S12: Wind speed distributions of SODAR and simulations at the times of available SODAR data) at (a) 50 m, (b) 100 m, (c) 200 m and (d) 300 m; Figure S13: Wind speed distributions for the CCLM data at the times of available SODAR data and for all the CCLM data at (a) 50 m, (b) 100 m, (c) 200 m and (d) 300 m; Figure S14: Statistics for strong LLJs (jet speed $\geq$ 15 m/s) from the CCLM simulations at Cape Baranova of the (a) jet height, (b) jet speed, (c) jet direction and (d) directional shear; Figure S15: Statistics of the LLJ heights

for channeled LLJs from the CCLM simulations at Cape Baranova for different upstream mountain Froude number classes; Figure S16: CCLM simulations of the mean sea level pressure and 10 m wind speed for the area of the Kara and Laptev Sea for days with channeling events with a duration $\geq$ 12 h at 200 m in height: (a) at Cape Baranova and (b) at grid point Shokalsky south; Figure S17: Simulated 99%-tile of the wind speed and mean wind vectors for speeds exceeding 10 m/s for the area of Shokalsky Strait for different seasons 2017–2020: (a) March–May and (b) September–November.

Author Contributions: Conceptualization, G.H.; Data curation, G.H., C.D. and A.M.; Formal analysis, G.H. and C.D.; Funding acquisition, G.H. and A.M.; Methodology, G.H.; Project administration, G.H.; Supervision, G.H. and A.M.; Visualization, G.H.; Writing—original draft, G.H.; Writing—review and editing, G.H., C.D. and A.M. All authors have read and agreed to the published version of the manuscript.

Funding: This research was funded by the Federal Ministry of Education and Research (BMBF) under grant 03F0831C in the frame of German–Russian cooperation "WTZ RUS: Changing Arctic Transpolar System (CATS)" and the Russian Ministry of Education and Science (project RFMEFI61619X0108). The publication was funded by the Open Access Fund of the University of Trier and the German Research Foundation (DFG) within the Open Access Publishing funding program.

Institutional Review Board Statement: Not applicable.

Informed Consent Statement: Not applicable.

Data Availability Statement: SODAR data are available on PANGAEA [38] and the model data will be also made available on PANGAEA. Radiosoundings and synoptic observations are available on the AARI Electronic archive of meteorological and upper-air observations (http://old.aari.ru/resources/d0031/archive/description.html (accessed on 15 April 2022)).

Acknowledgments: Thanks go to the CLM Community and the German Meteorological Service for providing the basic COSMO-CLM model. This work used resources of the Deutsches Klimarechenzentrum (DKRZ) granted by its Scientific Steering Committee (WLA) under project ID bb0474. Thanks go to the Russian team at Cape Baranova for the effort of performing the measurements for three years. We thank colleagues at GEOMAR Kiel and AARI for the logistical support in the framework of the inter-disciplinary CATS project. We thank Lukas Schefczyk for performing the CCLM simulations and Rolf Zentek for help with plotting the CCLM data. Model data processing was done with Climate Data Operators (CDO) (https://doi.org/10.5281/zenodo.3539275 (accessed on 15 April 2022)) and R software. The statistics were computed using R software and the R package pracma.

Conflicts of Interest: The authors declare no conflict of interest.

References

1. Werner, K. Year of Polar Prediction—Enhance observations to provide improved forecasts in polar regions. *Polarforschung* **2021**, *89*, 81–84. [CrossRef]
2. Shupe, M.D.; Rex, M.; Blomquist, B.; Persson, P.O.G.; Schmale, J.; Uttal, T.; Althausen, D.; Angot, H.; Archer, S.; Bariteau, L.; et al. Overview of the MOSAiC expedition—Atmosphere. *Elem. Sci. Anthr.* **2022**, *10*, 00060. [CrossRef]
3. Hori, M.; Inoue, J. Upper Atmospheric Soundings in Ice Base Cape Baranova during the YOPP Special Observing Period. *Polar Data J.* **2020**, *4*, 55–60. [CrossRef]
4. De Boer, G.; Dexheimer, D.; Mei, F.; Hubbe, J.; Longbottom, C.; Carroll, P.J.; Apple, M.; Goldberger, L.; Oaks, D.; Lapierre, J.; et al. Atmospheric observations made at Oliktok Point, Alaska, as part of the Profiling at Oliktok Point to Enhance YOPP Experiments (POPEYE) campaign. *Earth Syst. Sci. Data* **2019**, *11*, 1349–1362. [CrossRef]
5. Batrak, Y.; Müller, M. On the warm bias in atmospheric reanalyses induced by the missing snow over Arctic sea-ice. *Nat. Commun.* **2019**, *10*, 4170. [CrossRef] [PubMed]
6. Heinemann, G.; Willmes, S.; Schefczyk, L.; Makshtas, A.; Kustov, V.; Makhotina, I. Observations and Simulations of Meteorological Conditions over Arctic Thick Sea Ice in Late Winter during the Transarktika 2019 Expedition. *Atmosphere* **2021**, *12*, 174. [CrossRef]
7. Inoue, J.; Sato, K.; Rinke, A.; Cassano, J.J.; Fettweis, X.; Heinemann, G.; Matthes, H.; Orr, A.; Phillips, T.; Seefeldt, M.; et al. Clouds and radiation processes in regional climate models evaluated using observations over the ice-free Arctic Ocean. *J. Geophys. Res.* **2020**. [CrossRef]
8. Sedlar, J.; Tjernström, M.; Rinke, A.; Orr, A.; Cassano, J.; Fettweis, X.; Heinemann, G.; Seefeldt, M.; Solomon, A.; Matthes, H.; et al. Confronting Arctic troposphere, clouds, and surface energy budget representations in regional climate models with observations. *J. Geophys. Res.* **2020**, *126*, e2020JD033904. [CrossRef]

9. Preußer, A.; Heinemann, G.; Willmes, S.; Paul, S. Circumpolar polynya regions and ice production in the Arctic: Results from MODIS thermal infrared imagery from 2002/2003 to 2014/2015 with a regional focus on the Laptev Sea. *Cryosphere* **2016**, *10*, 3021–3042. [CrossRef]
10. Heinemann, G.; Drüe, C.; Schwarz, P.; Makshtas, A. Observations of Wintertime Low-Level Jets in the Coastal Region of the Laptev Sea in the Siberian Arctic Using SODAR/RASS. *Remote Sens.* **2021**, *13*, 1421. [CrossRef]
11. Tuononen, M.; Sinclair, V.A.; Vihma, T. A climatology of low-level jets in the mid-latitudes and polar regions of the Northern Hemisphere. *Atmos. Sci. Lett.* **2015**, *16*, 492–499. [CrossRef]
12. Heinemann, G. An Aircraft-Based Study of Strong Gap Flows in Nares Strait, Greenland. *Mon. Wea. Rev.* **2018**, *146*, 3589–3604. [CrossRef]
13. Samelson, R.M.; Barbour, P.L. Low-Level Jets, Orographic Effects, and Extreme Events in Nares Strait: A Model-Based Mesoscale Climatology. *Mon. Wea. Rev.* **2008**, *136*, 4746–4759. [CrossRef]
14. Moore, G.W.K.; Våge, K. Impact of model resolution on the representation of the air–sea interaction associated with the North Water Polynya. *Q. J. R. Meteorol. Soc.* **2018**, *144*, 1474–1489. [CrossRef]
15. Hersbach, H.; Bell, B.; Berrisford, P.; Hirahara, S.; Horányi, A.; Muñoz-Sabater, J.; Nicolas, J.; Peubey, C.; Radu, R.; Schepers, D.; et al. The ERA5 global reanalysis. *Q. J. R. Meteorol. Soc.* **2020**, *146*, 1999–2049. [CrossRef]
16. Gutjahr, O.; Heinemann, G. A model-based comparison of extreme winds in the Arctic and around Greenland. *Int. J. Climatol.* **2018**, *38*, 5272–5292. [CrossRef]
17. Kohnemann, S.H.; Heinemann, G. A climatology of wintertime low-level jets in Nares Strait. *Polar Res.* **2021**, *40*, 3622. [CrossRef]
18. Janout, M.A.; Hölemann, J.; Timokhov, L.; Gutjahr, O.; Heinemann, G. Circulation in the northwest Laptev Sea in the eastern Arctic Ocean: Crossroads between Siberian River water, Atlantic water and polynya-formed dense water. *J. Geophys. Res. Ocean.* **2017**, *122*, 6630–6647. [CrossRef]
19. Platonov, V.; Varentsov, M. Introducing a New Detailed Long-Term COSMO-CLM Hindcast for the Russian Arctic and the First Results of Its Evaluation. *Atmosphere* **2021**, *12*, 350. [CrossRef]
20. Anderson, P.S.; Ladkin, R.S.; Renfrew, I.A. An Autonomous Doppler Sodar Wind Profiling System. *J. Atmos. Ocean. Technol.* **2005**, *22*, 1309–1325. [CrossRef]
21. Rockel, B.; Will, A.; Hense, A. The Regional Climate Model COSMO-CLM (CCLM). *Meteorol. Z.* **2008**, *17*, 347–348. [CrossRef]
22. Spreen, G.; Kaleschke, L.; Heygster, G. Sea ice remote sensing using AMSR-E 89-GHz channels. *J. Geophys. Res.* **2008**, *113*, C02S03. [CrossRef]
23. Zhang, J.; Rothrock, D.A. Modeling Global Sea Ice with a Thickness and Enthalpy Distribution Model in Generalized Curvilinear Coordinates. *Mon. Wea. Rev.* **2003**, *131*, 845–861. [CrossRef]
24. Schröder, D.; Heinemann, G.; Willmes, S. The impact of a thermodynamic sea-ice module in the COSMO numerical weather prediction model on simulations for the Laptev Sea, Siberian Arctic. *Polar Res.* **2011**, *30*, 6334. [CrossRef]
25. Gutjahr, O.; Heinemann, G.; Preußer, A.; Willmes, S.; Drüe, C. Quantification of ice production in Laptev Sea polynyas and its sensitivity to thin-ice parameterizations in a regional climate model. *Cryosphere* **2016**, *10*, 2999–3019. [CrossRef]
26. Heinemann, G. Assessment of Regional Climate Model Simulations of the Katabatic Boundary Layer Structure over Greenland. *Atmosphere* **2020**, *11*, 571. [CrossRef]
27. Hastings, D.A.; Dunbar, P.K. Global Land One-kilometer Base Elevation (GLOBE) Digital Elevation Model, Documentation. *Key Geophys. Rec. Doc. (KGRD)* **1999**, *34*, 102–107.
28. Zentek, R. COSMO Documentation (Archived Version from 2019, Uploaded with Permission of the DWD). 2019. Available online: https://zenodo.org/record/3339384 (accessed on 8 June 2020).
29. Zentek, R.; Heinemann, G. Verification of the regional atmospheric model CCLM v5.0 with conventional data and lidar measurements in Antarctica. *Geosci. Model Dev.* **2020**, *13*, 1809–1825. [CrossRef]
30. Heinemann, G.; Zentek, R. A Model-Based Climatology of Low-Level Jets in the Weddell Sea Region of the Antarctic. *Atmosphere* **2021**, *12*, 1635. [CrossRef]
31. Kohnemann, S.H.E.; Heinemann, G.; Bromwich, D.H.; Gutjahr, O. Extreme Warming in the Kara Sea and Barents Sea during the Winter Period 2000–16. *J. Clim.* **2017**, *30*, 8913–8927. [CrossRef]
32. Platonov, V.; Kislov, A. High-Resolution COSMO-CLM Modeling and an Assessment of Mesoscale Features Caused by Coastal Parameters at Near-Shore Arctic Zones (Kara Sea). *Atmosphere* **2020**, *11*, 1062. [CrossRef]
33. Shestakova, A.A.; Repina, I.A. Overview of strong winds on the coasts of the Russian Arctic seas. *Ecol. Montenegrina* **2019**, *25*, 14–25. [CrossRef]
34. Barstad, I.; Adakudlu, M. Observation and modelling of gap flow and wake formation on Svalbard. *Q. J. R. Meteorol. Soc.* **2011**, *137*, 1731–1738. [CrossRef]
35. Sandvik, A.D.; Furevik, B.R. Case Study of a Coastal Jet at Spitsbergen—Comparison of SAR- and Model-Estimated Wind. *Mon. Wea. Rev.* **2002**, *130*, 1040–1051. [CrossRef]
36. Doyle, J.D.; Shapiro, M.A. Flow response to large-scale topography:the Greenland tip jet. *Tellus A* **1999**, *51*, 728–748. [CrossRef]
37. Gaberšek, S.; Durran, D.R. Gap Flows through Idealized Topography. Part I: Forcing by Large-Scale Winds in the Nonrotating Limit. *J. Atmos. Sci.* **2004**, *61*, 2846–2862. [CrossRef]
38. Heinemann, G.; Drüe, C. SODAR Wind Profiles at Cape Baranov 2017–2020. *PANGAEA* **2022**. [CrossRef]